Astronomy & Astrophysics manuscript no. highz˙201109
September 14, 2011

Faint high-redshift AGN in the Chandra Deep Field South: the evolution of the AGN luminosity function and black hole demography

F. Fiore[1], S. Puccetti[2], A. Grazian[1], N. Menci[1], F. Shankar[3], P. Santini[1], E. Piconcelli[1], A.M. Koekemoer[4], A. Fontana[1], K. Boutsia[1], M. Castellano[1], A. Lamastra[1], C. Malacaria[1,5], C. Feruglio[6], S. Mathur[7], N. Miller[8], and M. Pannella[9]

[1] Osservatorio Astronomico di Roma, via Frascati 33, I00040 Monteporzio Catone, Italy e-mail: fabrizio.fiore@oa-roma.inaf.it
[2] ASI Science Data Center, Italy
[3] Max-Planck-Institut fur Astrophysik, Germany
[4] Space Telescope Science Institute, USA
[5] Universita' di Roma La Sapienza, Italy
[6] Institut de RadioAstronomie Millimtrique, France
[7] Ohio State University, USA
[8] University of Maryland, USA
[9] CEA Saclay, Service d'Astrophysique, France

August 25, 2011

ABSTRACT

Context. We present detection and analysis of faint X-ray sources in the Chandra deep field south (CDFS) using the 4 Msec Chandra observation.
Aims. We put new constraints on the z=3–7 AGN luminosity function, its cosmological evolution and high-redshift black hole and AGN demography.
Methods. We use a new detection algorithm, using the entire 3-dimensional data-cube (position and energy), and use a targeted search at the position of high-z galaxies in the GOODS-South survey.
Results. This optimized technique results in the identification of 54 z>3 AGNs, 29 of which are new detections. Applying stringent completeness criteria, we derive AGN luminosity functions in the redshift bins 3–4, 4–5 and >5.8 and for 42.75<log L(2–10 keV)<44.5. We join this data with the luminous AGN luminosity functions from optical surveys and find that the evolution of the high-z, wide luminosity range luminosity function can be best modeled by pure luminosity evolution with L^* decreasing from 6.6×10^{44} ergs/s at z=3 to $L^* = 2 \times 10^{44}$ ergs/s at z=6. We compare the high-z luminosity function with the prediction of theoretical models using galaxy interactions as AGN triggering mechanism. We find that these models are broadly able to reproduce the high-z AGN luminosity functions. A better agreement is found assuming a minimum Dark Matter halo mass for black hole formation and growth. We compare our AGN luminosity functions with galaxy mass functions to derive high-z AGN duty cycle using observed Eddington ratio distributions to derive black hole masses. We find that the duty cycle increases with galaxy stellar mass and redshift by a factor 10-30 from z=0.25 to z=4-5. We also report on the detection of a large fraction of highly obscured, Compton thick AGN at z> 3 (18^{+17}_{-10}%). Their optical counterparts do not show any reddening and we thus conclude that the size of the X-ray absorber is likely smaller than the dust sublimation radius. We finally report the discovery of a highly star-forming galaxy at z=3.47, arguing that its X-ray luminosity is likely dominated by stellar sources. If confirmed, this would be one of the farthest objects in which stellar sources are detected in X-rays.

Key words. Galaxies: active – Galaxies: evolution – Galaxies: quasars – general

1. Introduction

The study of high redshift AGN holds the key to understand early structure formation and probe the Universe during its infancy. High-z AGN have been extensively used to investigate key issues such as the evolution of the correlations between the black hole mass and the galaxy properties (see e.g Lamastra et al. 2010 and references therein), the AGN contribution to the reionization, heating of the Inter-Galactic Matter and its effect on structure formation (e.g. Giallongo et al. 1997, Malkan et al. 2003, Hopkins et al. 2007, Cowie et al. 2010, Boutsia et al. 2011). However, there are other fundamental issues that can be tackled by studying high-z AGN: a) scenarios for the formation of the black hole (BH) seeds, which will eventually grow up to form the super-massive black holes (SMBHs) seen in most galaxy bulges. Two main scenarios have been currently proposed, the monolithic collapse of $10^4 - 10^5$ M$\odot$ gas clouds to BH (Lodato & Natarajan 2006, Lodato & Natarajan 2007, Begelman 2010, Volonteri & Begelman 2010), or early generation of $\sim$ 100 M$\odot$ BH produced by the supernova explosions of the first Pop III stars (Madau & Rees 2001). b) Investigate the physics of accretion at high-z: is

BH growth mainly due to relatively few accretion episodes, as predicted in hierarchical scenarios (see e.g. Dotti et al. 2010 and references therein), or by the so called chaotic accretion (hundreds to thousands of small accretion episodes, King et al. 2008)? The two scenarios predict different BH spin distributions, and thus different distributions for the radiative efficiency. c) Being BH the structures with the fastest (exponential) growth rate, they can be used to constrain both the expansion rate of the Universe and the growth rate of the primordial perturbation at high-z, i.e. competing cosmological scenarios (Fiore 2010, Lamastra et al. 2011). d) The slope of the high-z AGN luminosity function and of the SMBH mass function strongly depend on the AGN duty cycle, and therefore their measure can constrain this critical parameter. In turn, the AGN duty cycle holds information on the AGN triggering mechanisms. The evaluation of the evolution of the AGN duty cycle can thus help in disentangling among competing scenarios for AGN triggering and feeding. In this paper we discuss in more detail this last issue. Two main scenarios for AGN triggering and feeding have been investigated so far: galaxy encounters (Barnes & Hernquist 1996, Cavaliere & Vittorini 2000, Menci et al. 2006, Menci et al. 2008), and recycled gas produced by normal stellar evolution in the inner bulge (Ciotti & Ostriker 2007, Ciotti et al. 2010, Cen 2011). These make different predictions about the AGN time scale and duty cycle. In the former models nuclear activation follows galaxy interactions. Since these are naturally more frequent in the past, when, at the same time, more gas is available for nuclear accretion since it has not yet been locked in stars, this scenario predicts a strong increase of the AGN duty cycle with the redshift. In the recycled star gas scenario the AGN timescale is much longer, up to Gyr, although with decreasing Eddington ratio. A less extreme variation of the AGN duty cycle with the redshift is thus expected. One of the goals of this paper is to assess what can be already done with present AGN surveys to distinguish between these competing scenarios, and which kind of surveys should be planned to best assess the main AGN triggering and feeding mechanism.

Large area optical surveys such as the SDSS, the CFHQS, and the NOAO DWFS/DLS have already been able to discover large samples of z$>$ 4.5 QSOs (e.g. Richards et al. 2006, Glikman et al. 2011) and about 50 QSOs at $z > 5.8$ (e.g. Jiang et al. 2009, Willott et al. 2010a). The majority of these high-z AGN are broad line, unobscured, high luminosity AGN. They are likely the tips of the iceberg of the high-z AGN population. Lower luminosity and/or moderately obscured AGN can, in principle, be detected directly in current and future X-ray surveys. Dedicated searches for high-z AGN using both deep and wide area X-ray surveys and a multi-band selection of suitable candidates can increase the number of high-z AGN by a factor > 10. In particular, it should be possible to find hundreds rare high-z, high luminosity QSOs, in both the all sky and deep eROSITA surveys (the 0.5-2 keV flux limit of the all sky survey being the order of 10^{-14} erg/cm^2/s , while that of the deep survey, covering hundreds deg^2, should be 2-3 times deeper) with a selection function much less biased than optical surveys (recall that $\tau_X/\tau_{opt} \approx (1+z)^{-3.5}$, where τ_X and τ_{opt} are the optical depths in the observed-frame X-ray and optical bands, assuming no evolution of the dust-to-gas ratio). To constrain the faint end of the high-z AGN luminosity function, and therefore the shape of the luminosity function and of the SMBH mass function, we need to best exploit current and future deep surveys. Unfortunately, so far the number of X-ray selected AGN at z$>$ 3 in deep Chandra and XMM surveys is only of a few tens, and ∼half a dozen at z$>$ 4.5 (see e.g. Brandt et al. 2004, Fontanot et al. 2007, Brusa et al. 2009a, Brusa et al. 2009b, Civano et al. 2011). The difficulty in detecting directly high-z AGN in X-ray surveys suggests an alternative approach. Looking at the X-ray emission at the position of known sources allows one to use a less conservative threshold for source detection than in a blind search, and therefore to reach a lower flux limit. Furthermore, a highly optimized X-ray analysis tool is deemed mandatory to fully exploit the richness of the data produced by Chandra and XMM. To this purpose we developed a new X-ray detection and photometry tool (dubbed *ephot*, see the Appendix). In this paper we search for X-ray emission at the position of candidate high-z galaxies selected in the HST/WFC3 ERS (Early release science) area and in the GOODS area of the Chandra Deep Field South (CDFS) by using *ephot*. We use the new 4 Msec Chandra dataset, which represent the most sensitive X-ray exposure ever achieved. We first study selection effects affecting our candidate high-z AGN, and then join our CDFS samples to other X-ray and optically selected AGN samples at the same redshift to build AGN luminosity functions at z$>$ 3 over several luminosity decades. By assuming appropriate bolometric corrections and appropriate distributions of $\lambda = L_{bol}/L_{Edd}$ we convert these luminosity functions in SMBH mass functions. We then evaluate the stellar mass functions of *active* galaxies by converting the SMBH mass to galaxy stellar mass by using the *Magorrian* relationship (Ferrarese & Ford 2005, Shankar et al. 2009a and references therein). Finally we estimate the AGN duty cycle as a function of the redshift by dividing the stellar mass function of *active* galaxies by the stellar mass function of *all* galaxies at the same redshift. The AGN duty cycle as a function of the redshift is then compared with the expectation of models for structure formation using galaxy interaction as AGN triggering mechanism. A $H_0 = 70$ km s^{-1} Mpc^{-1}, Ω_M=0.3, $\Omega_\Lambda = 0.7$ cosmology is adopted throughout.

2. Candidate high-z galaxy samples

We built a catalog of z$>$ 3 galaxy candidates in the GOODS south and ERS fields including:

- all galaxies with high quality spectroscopic redshift > 3;
- all galaxies with 68% limit of photometric redshift > 3;
- all galaxies with B-V vs V-I or V-H colors suggesting 3.5$<$z$<$4.4;
- all galaxies with V-I vs I-Z or I-H colors suggesting 4.4$<$z$<$6.0;
- all galaxies with I-Z vs Z-Y or Z-Y vs Y-J colors suggesting z$>$6;
- all galaxies with Y-J vs J-H colors suggesting z$>$8.

2.1. GOODS field

We use the GOODS-MUSIC catalog (Grazian et al. 2006, Santini et al. 2009), based on the mosaics reduced as described in Koekemoer et al. (2011), see also Windhorst et al.

(2011), which includes galaxies selected in the HST/ACS z band and Spitzer/IRAC 4.5μm band. 190 GOODS-MUSIC galaxies have a high quality optical or near-infrared spectrum confirming that they are z> 3 galaxies, 26 have a spectroscopic confirmation at z> 5. 4284 galaxies without high quality spectroscopic redshift z_{spec} have photometric redshift $z_{phot} > 3$, considering the 68% upper limit. To this sample, we added 171 galaxies without high quality z_{spec} and $z_{phot} < 3$ that lie in the 3.5<z<4.4 region of the ACS B-V vs V-I diagram and 143 galaxies that lie in the 4.4<z<6.0 region of the ACS V-I vs I-Z diagram. The total number of high-z galaxy candidates considered is thus 4788. About 10% of these galaxies lie within a few arcsec from an X-ray source previously identified with a low-z AGN or galaxy or galaxy cluster. These objects were conservatively excluded from the list, leaving us with about 4300 high-z galaxy candidates.

2.2. ERS field

We use the GOODS-ERS catalog (Grazian et al. 2010, Santini et al. 2011), which includes 2291 galaxies selected in the HST/WFC3 H band and with photometric redshift >3. 42 of these objects have a confirmed spectroscopic redshift (only 2 with z> 5). Again, about 10% of these galaxies lie close to bright X-ray sources, thus limiting the ERS candidate high-z galaxy sample to about 2000 galaxies.

There is of course an overlap between the GOODS-ERS and the GOODS-MUSIC catalogs (the GOODS field covers nearly completely the ERS field). Of the 2291 GOODS-ERS, z> 3 galaxies 570 are present in the GOODS-MUSIC catalog and in 420 cases the GOODS-MUSIC photometric redshift is > 3 Therefore, these objects are present also in the GOODS-MUSIC high-z galaxy candidate sample.

2.3. Additional samples

We also considered 330 z> 6 galaxy candidates from the lists of Bouwens et al. 2006, Castellano et al. 2010, McLure et al. 2010, McLure et al. 2011, Bouwens et al. 2010, which are not included in the above two lists.

3. Multiwavelength properties of High-z AGN and galaxies in the CDFS.

To extract statistically quantitative information from a given sample of "detected" sources in an X-ray image, we need to assess its reliability (i.e. number of spurious detections) and completeness. To both purposes we run a series of extensive detection runs on simulated data, see the Appendix for details. We choose a detection threshold corresponding to 1 spurious detection in 5000 candidates, i.e. about 1 spurious detection in the GOODS-MUSIC sample and <1 spurious detection in the GOODS-ERS sample. We detect 17 sources at z> 3 from the GOODS-ERS catalog and 41 from the GOODS-MUSIC catalog within this threshold. As an example, Fig. 1 show the B, z and H band images of three Chandra-GOODS-ERS sources. Table 1 and 2 give position, redshift, X-ray band that optimizes the detection, 0.5-2 keV flux, z band and H band magnitudes and 4.5μm fluxes for the GOODS-ERS and GOODS-MUSIC X-ray

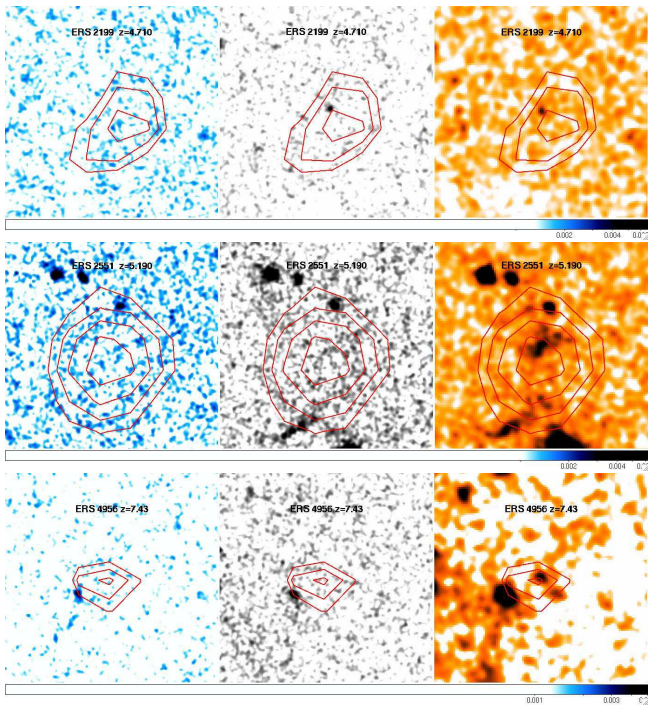

Fig. 1. HST ACS B band (left panel), z band (central panel) and HST WFC3 H band (right panel) images of three Chandra-GOODS-ERS sources with overlaid X-ray contours in the 0.7-2.7 keV band (E2199), 0.7-1.9 keV band (E2551) and 0.4-1.5 keV band (E4956)

detected sources, along with a few sources just below detection threshold (4 from the ERS-GOODS sample, 2 from the GOODS-MUSIC). We do not detect any of the candidate $z \gtrsim 6$ galaxies in Bouwens et al. 2006, Castellano et al. 2010, McLure et al. 2010, McLure et al. 2011, Bouwens et al. 2010. One of these galaxies has an X-ray counterpart just below threshold (also reported in Table 2). At the position of this source there are 11 counts in the band 0.4-0.8 keV ($\sim$ 3 of which are background counts) in a 2 arcsec radius region. If the 0.4-0.8 keV emission is due to iron Kα emission at 6.4 keV the redshift would be $\gtrsim 8$, which is inconsistent with the detection in the z band. Because of these uncertainties we do not discuss further this source.

Five Chandra-GOODS-ERS sources are present in the 2 Msec direct detection list of Luo et al. 2008 (Luo08 hereafter, search within a circle of 1 arcsec radius). Three of them have z_{phot} in Luo et al. 2010 (Luo10 hereafter) consistent with those in the GOODS-ERS catalog, while in one case the Luo10 z_{phot} is just below 3. One Chandra-GOODS-ERS source is confused/blended in the Luo08 catalog. Eight Chandra-GOODS-ERS sources are present in the 4 Msec direct detection list of Xue et al. 2011 (Xue11 hereafter). Two of the three Xue11 sources not in the Luo08 catalog have a photometric redshift, and this is > 3 in both cases. 16 Chandra-GOODS-MUSIC sources are present in the Luo08 list, 13 with photometric or spectroscopic redshift consistent with those in the GOODS-MUSIC catalog. Three additional sources are present in the Xue11 catalog, two of them have a photometric redshift, and this is consistent with that in the GOODS-MUSIC catalog. Source

M208 was not detected by Luo08, while it is now detected by Xue11. It is extensively discussed in Gilli et al. 2011.

The accuracy of the photometric redshifts is greatly improved thanks to the near infrared bands covered by WFC3 (see Table 1 and 2). The WFC3 coverage also increases the high-z candidate galaxy X-ray detection rate. The ERS area is less than one third of the full GOODS area, and therefore, based on the Chandra-GOODS-ERS detections, one would expect $\gtrsim$54 detections in GOODS-MUSIC, while only 41 have been actually found. Only half of the Chandra-GOODS-ERS detections have a counterpart in the GOODS-MUSIC catalog. 31% and 40% of the Chandra-GOODS-MUSIC detections are also present in the Luo08 2 Msec and Xue11 catalogs. 28% and 47% of the Chandra-GOODS-ERS detections are present in the same catalogs. We study in more detail the different Chandra-GOODS-MUSIC and Chandra-GOODS-ERS selection effects in section 3.3.

3.1. X-ray and optical spectroscopy

We discuss here X-ray and optical spectroscopy of our X-ray sources. Unfortunately only one of the 17 sources in the Chandra-GOODS-ERS sample has optical spectroscopy available. On the other hand, 11 of the 41 sources of the Chandra-GOODS-MUSIC sample have optical spectroscopy available. To exploit this rather large dataset we complement the full Chandra-GOODS-ERS sample, with the Chandra-GOODS-MUSIC sources with optical spectroscopy[1].

X-ray spectra have been extracted from the merged event file using source extraction regions of 2-6 arcsec radius, depending on the source off-axis (the Chandra Point Spread Function degrades quickly with the off-axis angle). Background spectra have been extracted from nearby source-free regions. We also used the total background spectra at three off-axis angles (see the Appendix for details). Background spectra are then normalized to the source extraction region area. We report in Table 3 the results of fitting a simple power law model to the data. Several Chandra-GOODS-ERS and Chandra-GOODS-MUSIC sources have flat X-ray spectra, strongly suggesting the presence of large absorbing column densities along those lines of sight. The quality of the spectra is poor, however in several cases the statistic is good enough to perform a proper fit with a model including an absorbed power law or a reflection spectrum. In the following we briefly outline the main results from this analysis.

- E537 shows an extremely hard spectrum. A simple power law fit produces a negative slope of $\Gamma \sim$ -0.15. An absorbed power-law model with Γ fixed to 1.8 yields a column density of N_H=1.6 $\times$ 10^{24} cm^{-2}. A better description of the spectral shape of the low energy spectrum is obtained by adding an unabsorbed power law (see Fig. 2). Such component typically provides an excellent fit of the X-ray spectrum of many well-studied obscured AGNs and its origin is explained in terms of emission due to reprocessing of the nuclear continuum by surrounding material and/or a portion of primary radiation leaking through the absorber (see e.g. Turner et al 1997, Piconcelli et al. 2007). The photon index of the soft X-ray component is fixed to Γ=1.8, while the resulting ratio between the normalization of the unabsorbed and absorbed power law is $\sim$0.02. An alternative model consisting of a Compton reflection emission component (`pexrav` model in XSPEC) obscured by a column density of $N_H = 5\pm2 \times 10^{23}$ cm^{-2} is statistically equivalent.
- The X-ray spectrum of M4835 reveals additional complexity when fitted with a simple absorbed ($N_H = 9\pm2 \times 10^{23}$ cm^{-2}) power-law model (C-stat/dof=425/442). The best-fit model to the *Chandra* data includes an additional component due to X-ray reflection from cold circumnuclear matter. In this case the primary continuum is obscured by a column density of $N_H \sim 1.5^{+0.4}_{-0.8} \times 10^{24}$ cm^{-2} and the normalization of the nuclear component is about 5 times larger than that of the reflection component. Finally, the limit equivalent width (EW) of the Fe Kα emission line measured with respect to the reflection continuum is <1.1 keV, i.e. still consistent with the expectation of a reflection model. Fig. 2 shows the Chandra spectrum of M4835 fitted by this reflection + transmission model.
- M5390 is G202, the well-known, highly obscured QSO discovered by Norman et al. 2002 at $z = 3.7$. The Chandra spectrum is consistent with the XMM one presented by Comastri et al. 2011. It is well fitted by a power law model (with $\Gamma = 1.8$ fix) absorbed by a column density of $N_H \sim 1.2\pm0.15\times10^{24}$ cm^{-2} and gaussian line (E=6.6 keV, likely a blend of the 6.4 keV neutral Fe and 6.7 keV Fe XXV Kα lines, EW=0.8$\pm$0.4 keV), plus an energetically unimportant soft component. The quality of the fit decreases if the continuum is modeled with a pure reflection component.
- M208 is the source presented by Gilli et al. 2011, and we confirm the results reported in that paper, finding the spectrum consistent with being obscured by a Compton thick absorber. Very similar results are obtained for E1577, which is best fitted by a heavily absorbed (i.e. $N_H \geq 10^{24}$ cm^{-2}) power law model (see Fig. 2). We also find the presence of obscuration with column density values consistent with 10^{24} cm^{-2} in the spectrum of E8479.
- Large N_H values exceeding 10^{23} cm^{-2} (but still in the Compton-thin regime) are reported from the spectral analysis of E1617, M8273, M4302 and M3320. Remarkably, in the spectrum of the latter source at z=3.471, we find clear evidence of an emission line with an EW = 160$\pm$100 eV at a best-fit rest-frame energy of 6.97 keV and, therefore, associated with highly ionized (i.e. Fe XXVI) iron.

In conclusion, at least 3 of the 17 Chandra-GOODS-ERS sources are likely to be Compton thick AGN, which is 18^{+17}_{-10}% of the AGN in the sample are Compton thick, as well as 4 of the 11 Chandra-GOODS-MUSIC AGN with spectroscopic redshift (one of these sources is in common with the Chandra-GOODS-ERS sample). Other 3 Chandra-GOODS-MUSIC and 1 Chandra-GOODS-ERS AGN are highly obscured. The luminosity of the Compton thick ERS and GOODS-MUSIC AGN is in the range log(L2-10keV)=43.5-44.5, i.e. between bright Seyfert 2

[1] We do not discuss here the rest of the Chandra-GOODS-MUSIC sample because it is affected by incompleteness, see next section, and because the quality of the photometric redshift is worse than that of the GOODS-ERS sample

Table 1. Chandra detected GOODS-ERS z> 3 galaxies

ID	RA	Dec	z	$E_{min-max}$	SNR	F(0.5-2keV)	zm	H	other ID[a]
	J2000	J2000		keV		erg/cm^2/s			
E537	53.082535	-27.755245	4.29 (2.9-4.5)	1.3-6.3	13.6	1.2E-16	25.48	24.21	L184, X275, M70139[b]
E737	53.050343	-27.752138	4.14 (4.0-4.4)	1.0-2.0	3.4	4.5E-17	25.65	24.94	X177, M70131[c]
E1312	53.016602	-27.744848	3.48 (3.4-3.6)	0.9-2.1	5.6	1.0E-16	25.30	24.39	L68, X100, M13365[d], MY5063
E1516	53.119888	-27.743042	4.29 (4.1-6.9)	0.5-1.9	3.4	3.2E-17	27.99	25.57	X392, M70099
E1577	53.020576	-27.742151	3.462 spec.	1.9-6.3	3.7	9.5E-17	23.62	23.35	M13549,MY51260
E1617	53.010651	-27.741613	3.38 (3.3-3.4)	0.9-3.8	7.7	1.9E-16	26.33	24.58	L61[e],X90
E2199	53.054756	-27.736839	4.71 (4.5-5.2)	0.7-2.7	2.9	3.5E-17	27.15	27.08	
E2309	53.117855	-27.734295	3.61 (3.3-3.8)	0.3-4.0	5.3	4.7E-17	23.81	22.93	L252, X386, M14078
E2498	53.006237	-27.734076	6.62 (5.9-7.3)	1.0-5.3	5.0	5.1E-17	-28.89	26.61	L57[f], X85
E2551	53.158340	-27.733500	5.19 (5.1-5.5)	0.7-1.9	4.3	5.0E-17	-27.59	25.00	G557,L323,X521,M70091
E2658	53.055538	-27.732950	3.74 (3.5-4.1)	0.4-6.0	3.8	4.2E-17	26.84	26.85	
E4956	53.037708	-27.711536	7.43 (>7.0)*	0.4-1.5	3.2	6.3E-17	-29.20	26.97	
E5165	53.038258	-27.709778	3.87 (3.6-4.2)	0.5-2.0	3.3	7.0E-17	26.80	26.94	L100[g]
E6257	53.168419	-27.719418	3.22 (3.2-3.5)	0.8-1.9	3.1	4.1E-17	24.64	24.56	X554, M15144/M15156[h], MY
E7911	53.194885	-27.699949	4.86 (4.7-5.4)	0.8-1.8	3.2	1.3E-16	99.00	25.68	
E8479	53.167572	-27.694883	3.67 (3.3-3.9)	1.5-3.2	3.2	7.0E-17	26.56	26.27	MY58818
E10247	53.131218	-27.685293	3.95 (3.6-4.0)	0.5-4.5	3.1	3.2E-17	26.55	26.59	
E1611[h]	53.079372	-27.741625	6.91 (6.0-7.4)	0.8-1.7	2.6	2.5E-17	26.15	23.75	M70107
E7840[h]	53.173592	-27.661259	3.68 (3.3-4.0)	0.3-6.3	2.9	4.9E-16	25.04	25.44	MY64565
E8439[h]	53.183681	-27.694748	4.91 (4.8-5.2)	0.8-2.5	2.9	3.2E-17	99.00	25.26	
E9850[h]	53.102806	-27.679691	3.93 (3.8-4.1)	0.9-4.7	2.9	2.1E-16	26.36	26.46	

[a]L=Luo08, M=GOODS-MUSIC, MY=GOODS-MUSYC Cardamone et al. 2010;X=Xue11; [b]GOODS-MUSIC z=2.28; [c]GOODS-MUSIC z=2.33; [d]no redshift in GOODS-MUSIC catalog; [e]Luo10 z=2.123; [f]Luo10 z=2.808; [g]Luo08 confused with optically bright galaxy; [h]M15144 z=0.15 M15156 z=3.07; *secondary solution at z∼2;[h] just below detection threshold.

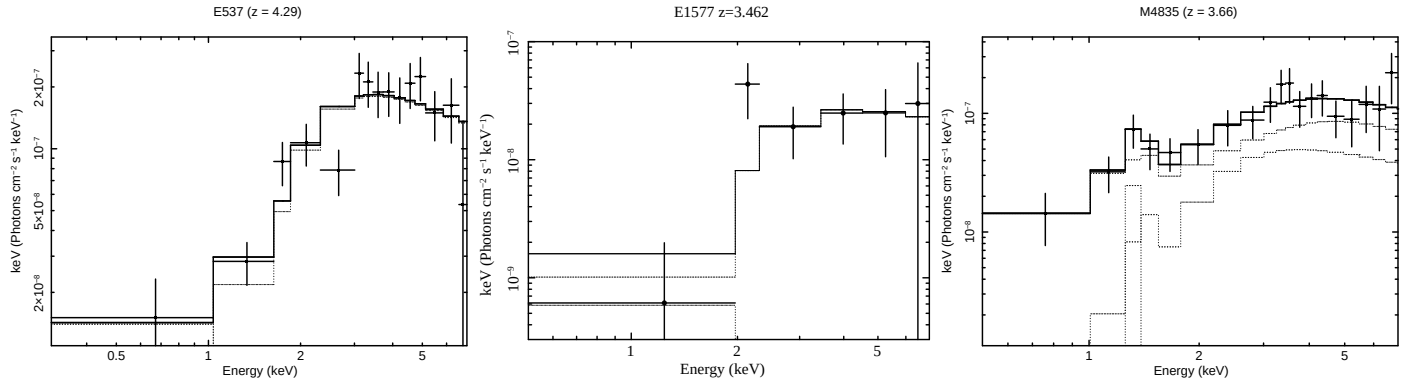

Fig. 2. The Chandra X-ray spectra of E537 [Left panel], E1577 [central panel], and M4835 [Right panel].

galaxies and type 2 QSOs. The 2-10 keV flux of the Chandra-GOODS-ERS sources is between 0.3 and 3×10^{-16} erg/cm^2/s . At this fluxes the Gilli et al. 2007 model for the Cosmic X-ray background (CXB) predicts a fraction of Compton thick AGN of $\sim$ 20%. This is already similar to the fraction of Compton thick AGN we find at z> 3, thus suggesting that Compton thick AGN are probably more common at high-z than previously predicted (also see Gilli et al. 2011).

It is instructive to compare the result of the X-ray spectroscopy to those of the optical spectroscopy, photometry and morphology in Table 3. The two CT AGN for which CIV is redshifted in the band covered by optical spectroscopy show a narrow CIV, in addition to narrow Lyα. One of these (E1577/M13549) also shows broad absorption blueward CIV. The highest redshift CT AGN (M208) shows a narrow Lyα and a relatively broad (2000km/s) NV emission (also see Gilli et al. 2011). Two of the three highly obscured AGN (M3320 and M8273) also show narrow Lyα emission and, when redshifted in the band covered by the spectroscopy, narrow CIV. In the spectrum of the third highly obscured source (M4302) strong and broad absorption lines are present.

Four of the ten highly obscured and Compton thick AGN have a point like morphology in the z band (M13549/E1577, M5390, M4302, M208) or H band (E1577) based on CLASS_STAR parameter of SEXTRACTOR, FWHM measurements, and eye-ball inspection of z and H band images. This suggests that the active nucleus contributes significantly to the UV and optical rest-frame emission, as further confirmed in M4302 and M13549/E1577 by the detection of likely nuclear broad absorption lines in their UV rest frame spectra.

We estimated the rest-frame UV (0.16μm) extinction of the highly obscured and Compton thick AGN by fitting their observed Spectral Energy Distribution with galaxy templates and the Calzetti et al. 2000 extinction law. Table 3 gives the 1σ upper limit to A(0.16μm) along with the

Table 2. Chandra detected GOODS-MUSIC z> 3 galaxies

ID	RA	Dec	z	$E_{min-max}$	SNR	F(0.5-2keV)	zm	H	F(4.5μm)	other ID[a]
	J2000	J2000		keV		erg/cm^2/s			μJy	
M208[b]	53.122036	-27.938740	4.762 spec.	1.1-4.0	3.6	1.0E-16	24.99	23.42	3.0	G618,X403,M
M387	53.088505	-27.933449	3.130 (2.4-3.5)	0.5-1.3	2.7	6.7E-17	25.02	99.00	1.1	
M603	53.109451	-27.928093	3.360 (2.2-3.9)	0.8-1.9	2.9	3.7E-17	25.82	25.09	0.5	MY21391
M2690	53.163532	-27.890448	3.620 (1.5-4.6)	0.7-6.0	3.0	1.1E-16	25.67	24.96	9.1	MY27345
M3268	53.083511	-27.881855	3.300 (2.6-3.8)	1.7-6.3	3.2	1.0E-16	26.46	26.47	0.2	MY28191
M3320	53.209370	-27.881086	3.470 spec	0.7-5.0	41.1	2.5E-15	25.29	99.00	4.5	G159, L402,X
M3323	53.184639	-27.880917	3.471 spec.	0.5-2.1	12.7	4.5E-16	23.98	23.84	4.0	G21,L369,X5
M4302	53.174389	-27.867350	3.610 spec.	0.4-5.0	30.6	1.5E-15	22.43	22.44	9.6	MY30943,G2
M4417	53.097237	-27.865793	3.470 spec	0.5-3.2	3.1	2.2E-17	23.33	23.15	2.5	MY31136
M4835	53.078468	-27.859852	3.660 spec.	0.8-6.3	12.4	1.2E-16	25.08	99.00	7.3	G263b,L180,
M5390[c]	53.124371	-27.851633	3.700 spec.	0.7-6.3	18.5	2.3E-16	24.62	23.44	6.8	G202,L265,X
M5522	53.157639	-27.849911	3.690 (2.7-4.1)	0.3-3.0	3.0	2.4E-17	25.41	24.31	1.2	MY33385
M5842	53.070236	-27.845531	3.830 (2.8-4.3)	0.7-1.8	3.5	3.2E-17	25.20	24.68	3.5	X235, MY34
M7305	53.072567	-27.827642	3.440 (3.1-3.7)	0.9-1.8	3.5	3.5E-17	24.37	24.45	1.7	
M8039	53.034122	-27.817532	3.190 (2.5-3.9)[d]	0.5-5.0	3.1	1.7E-17	26.95	-26.24	0.1	MY38702
M8273	53.165268	-27.814058	3.064 spec.	0.9-6.3	31.5	8.0E-16	24.51	22.40	16.7	MY39298,G2
M8728	53.069000	-27.807203	4.820 (3.9-5.5)	0.8-2.2	3.1	5.4E-17	26.58	-26.24	0.7	
M9350	53.167900	-27.797960	3.360 (3.2-3.5)	0.4-3.6	3.1	1.7E-17	24.76	24.74	0.8	MY41761
M9363	53.051006	-27.797874	3.610 (3.0-4.1)[d]	1.3-4.0	3.2	8.4E-17	26.82	-26.24	0.1	
M10390	53.059620	-27.784552	3.210 (2.4-3.7)	0.3-3.6	2.8	2.0E-17	26.32	24.90	1.0	
M10429	53.178471	-27.784035	3.193 spec.	0.4-4.5	22.7	7.6E-16	25.18	24.08	2.0	MY44068,L3
M10515	53.143574	-27.783009	5.260 (1.8-6.6)	1.0-6.0	3.3	7.3E-17	25.40	23.42	21.1	
M10548	53.021168	-27.782366	4.823 spec.	0.4-1.9	3.2	4.4E-17	23.71	99.00	3.4	MY44369
M13473	53.171535	-27.743347	3.210 (2.6-3.8)[d]	0.6-1.8	3.1	2.6E-17	24.80	24.23	0.7	MY50924
M13549	53.020576	-27.742151	3.462 spec.	1.9-6.3	3.7	1.2E-16	23.69	23.33	3.5	MY51260,E1
M14078	53.117867	-27.734310	3.560 (2.8-3.8)	0.3-4.0	5.2	4.7E-17	23.97	22.69	19.9	E2309,L252,X
M70091	53.158215	-27.733717	3.200 (2.0-5.4)	0.9-2.0	4.2	4.2E-17	27.65	24.55	5.3	E2551,G557,
M70099	53.119797	-27.743099	6.220 (> 2.9)	0.5-1.9	3.7	3.7E-17	27.10	24.91	6.2	X392,E1516
M70168	53.111530	-27.767839	5.010 (2.0-6.5)	0.8-4.7	11.1	1.3E-16	25.97	-25.03	2.3	G518,L245,X
M70340	53.040970	-27.837717	3.900 (> 3.9)	0.4-4.2	9.2	1.1E-16	-27.56	-25.46	2.2	G537,L103[e],
M70385	53.107418	-27.855694	3.980 (1.1-4.7)	0.6-2.0	7.3	1.2E-16	26.49	-25.26	4.1	G589,L235[f],
M70390	53.085411	-27.858023	4.180 (2.2-4.8)	0.5-1.7	3.8	3.8E-17	26.20	23.98	5.7	L191,X285
M70407	53.064629	-27.862434	5.900 (>1.8)	0.9-1.9	2.8	2.8E-17	27.02	24.89	1.5	
M70429	53.137917	-27.868238	3.630 (1.2-4.8)	0.4-3.4	9.7	1.5E-16	-27.90	25.41	2.3	G217a,L290[g]
M70435	53.215118	-27.870247	3.230 (>2.0)	0.7-6.0	9.8	1.2E-16	26.88	24.06	4.9	G508,L404,X
M70437	53.146461	-27.870945	4.420 (>2.7)	1.4-5.3	7.7	3.9E-17	27.62	-25.35	3.5	L306[h],X485
M70467	53.124233	-27.882565	4.250 (>2.0)	0.9-3.8	3.0	1.8E-17	26.85	-25.50	3.9	
M70481	53.189320	-27.888466	4.080 (3.3-4.5)	0.3-6.7	2.9	1.1E-16	26.75	24.02	8.0	
M70508	53.210999	-27.907394	3.180 (2.0-4.0)	0.3-5.7	4.6	9.7E-17	26.24	99.00	7.5	
M70525	53.136761	-27.917326	3.280 (0.8-3.8)	0.9-6.7	3.1	1.2E-16	-27.87	24.26	3.7	
M70531	53.151512	-27.926792	3.260 (>1.9)	1.7-4.5	3.0	1.1E-16	26.07	23.27	19.7	
M3607[h]	53.215858	-27.876823	3.468 spec	1.0-3.8	2.9	8.5E-17	24.93	99.00	0.9	
M70107[h]	53.079334	-27.741474	3.356 spec	0.8-4.7	3.4	2.1E-17	26.85	23.77	12.8	E1611
216554[i,h]	53.068958	-27.684222	$\gtrsim$6.0	0.4-0.8	2.4	1.4E-5[l]	25.8	–	–	

[a]L=Luo08, M=GOODS-MUSIC, MY=GOODS-MUSYC Cardamone et al. 2010;X=Xue11,G=Giacconi et al. 2002; [b] Gilli et al. 2011; [c] Norman et al. 2002; [d]secondary solution at z<0.5; [e] Luo08 z=2.45; Luo08[f] 2.71; [g] Luo08 z=2.36; [h] Luo08 z> 7.4; [h] just below detection threshold; [i] Bouwens et al. 2006; [l] count rate.

A(0.16μm) lower limit obtained using the 1σ lower limit to the neutral gas absorption column density and assuming a Galactic dust-to-gas ratio. We also plot for these sources the best fit N_H and A(0.16μm) upper limits in Fig. 3. We see that N_H measurements and the A(0.16μm) limits of all ten highly obscured or Compton thick AGN are completely inconsistent with a Galactic dust-to-gas ratio. This is true also for the four objects with point like morphology. The same conclusion is reached by estimating dust extinction from the galaxy stellar masses. It is difficult to estimate accurate stellar masses for our high-z AGN, but they likely exceed several 10^{10} $M_\odot$. The extinction expected based on the correlations found by Pannella et al. 2009 in a sample of z$\sim$ 2 BzK galaxies is of 3-6 magnitudes at 1500 Å . We conclude that, at least for the four point-like objects, the dust-to-gas ratio of the absorbing matter is likely 1/100-1/1000 that of the Galaxy. This is also lower than in the (mostly low-z) AGN studied by Maiolino et al. 2001, and Shi et al. 2006. The low dust-to-gas ratio may be explained if the absorbing matter is within of close to the dust sublimation radius. The other six highly obscured or Compton thick AGN have extended morphologies in the z and H images, suggesting that young stellar populations significantly contribute to the UV and optical rest frame emission. In these cases little can be said about the nuclear extinction and the dust-to-gas ratio.

Table 3. Multiwavelength properties of $z > 3$ galaxies

ID	Γ X-ray	logL(2-10keV) ergs/s	X-ray obsc.[a]	F(1.4GHz) μJy	SFR $M_\odot$/yr	Morph.[b] H band	A(0.16) SED	A(0.16) X-ray	Optical spec.
E537	-0.15±0.2	43.8	CT	19.6±6.2	730±230	E	< 2.6	> 1000	
E737	1.6±1.0	43.1		15.0±6.2	360±150	E			
E1312	1.2±0.7	43.7				P			
E1516	$3.0^{+2.0}_{-1.4}$	42.8		17.8±6.4	660±240	E			
E1577	$-0.9^{+0.9}_{-1.4}$	43.6	CT			P	< 1.1	> 930	Em.: Lyα narrow, CIV Abs.: CIV broad
E1617	0.9±0.3	44.4	HO			E	< 2.6	> 190	
E2199	1.6±1.3	42.9				P			
E2309	1.7±0.7	42.9				E			
E2498	0.9±0.5	43.9		16.3±6.4	1500±590	E			
E2551	1.8±0.7	43.2		33.5±6.4[g]	1870±360	E			
E2658	0.3±1.4	42.8				P			
E4956	2.2±0.9	43.9				E			
E5165	1.8±0.8	43.2				E			
E6257	1.5±1.5	42.8				E			
E7911	1.5±1.0	43.6				P			
E8479	-0.1±0.9	43.5	CT			E	< 1.1	> 470	
E10247	–	43.1				E			
ID	Γ X-ray	logL(2-10keV) ergs/s	X-ray obsc.[a]	F(1.4GHz) μJy	SFR $M_\odot$/yr	Morph.[b] z band	A(0.16) SED	A(0.16) X-ray	Optical spec.
M208[c]	0.1±0.6	44.0	CT	19.4±6.5	900±300	P	< 2.0	> 780	Em: Lyα narrow, NV bro
M3320	1.12±0.06	44.8	HO			E	< 3.5	> 120	Em.: Lyα narrow
M3323	1.6±0.21	43.8				P			Em.: Lyα broad
M4302	1.33±0.08	44.4	HO	17.6±6.1	450±160	P	< 1.8	> 110	Em.: Lyα, Lyβ, Lyγ, Abs: NV, CII, OI broad
M4417[d]	1.8±1.0	42.5		15.3±6.3	360±150	E			Abs: CIV, SiII, SiIV, CII, OI, SiII
M4835	0.08±0.24	44.0	CT	36.0 ± 6.2[g]	960±160	E			Em.: Lyα, CIV narrow
M5390[e]	0.18±0.16	44.3	CT	19.4 ± 6.1	530±170	P	< 1.1	> 820	Em.: Lyα, CIV, OVI, NV, CIV, HeII narrow
M8273	0.29±0.10	44.8	HO	49.6 ± 6.2[g]	900±110	E	< 2.0	> 380	Em.: Lyα, CIV narrow
M10429	1.40±0.10	44.0				P			Em.: CIV broad
M10548	2.75±1.30	43.0				E			Em.: Lyα narrow, noisy
M13549[f]	$-0.9^{+0.9}_{-1.4}$	43.6	CT			P			Em.: Lyα narrow, CIV, Abs: CIV broad

[a] CT=Compton thick ($N_H \gtrsim 10^{24}$ cm^{-2}); HO=Highly obscured, Compton thin,($10^{23} \lesssim N_H \lesssim 10^{24}$ cm^{-2}); [b] Morphology, P=point like, E=Extended; [c] Gilli et al. (2011); [d] Maiolino et al. 2008, [OII], [OIII] Hβ [e] Norman et al. (2002); [f]=E1577; [g]VLA-CDFS DR2 flux

3.2. Radio counterparts and star-formation rates

Two Chandra-GOODS-ERS sources (E2551 and E1611/M70107) and other five Chandra-GOODS-MUSIC sources (M2690, M4835, M8273, M70091 and M70340) have a detection at 1.4 GHz in the DR2 catalog of the VLA-CDFS survey Miller et al. 2008. Radio fluxes for the Chandra-GOODS-ERS sources and the Chandra-GOODS-MUSIC sources with spectroscopic redshift are given in Table 3. Other 8 sources in Table 3 have a faint radio signal at the position of the galaxy (signal to noise between 2.4 and 3.2). The probability that this signal is a background fluctuations is < 2%, corresponding to < 1 spurious radio detection in the full sample of sources in Table 3. We report in Table 3 radio fluxes also for the additional 8 faint detections. We stress that the latter faint fluxes may over-estimate the real radio flux because of the Eddington bias. A more robust average flux can be obtained by stacking together the radio images at the position of the X-ray sources. The average flux for the Chandra-GOODS-ERS and Chandra-GOODS-MUSIC sources without a detection in the DR2 VLA-CDFS catalog is 6.5±1.5μJy and 10.1±1.1μJy respectively.

The observed radio fluxes can be due to both nuclear and stellar processes. Using the La Franca et al. 2011 probability distributions for the X-ray to radio nuclear luminosity we would expect a L(2-10keV)/L(1.4 GHz) ratio $< 3 \times 10^4$ for $\sim 25\%$ of the sources in Table 3, and L(2-10keV)/L(1.4 GHz)$< 10^3$ for 5% of the sources. We converted the radio fluxes in Table 3 into luminosities by using the following expression:

$$L(1.4\mathrm{GHz}) = 1.19 \times 10^{20} DL^2 f(1.4\mathrm{GHz})(1+z)^{(\alpha-1)} \quad (1)$$

where DL is the luminosity distance in Mpc and $f(1.4\mathrm{GHz})$ is in μJy and we used $\alpha = 0.7$. We find in all cases L(2-10keV)/L(1.4 GHz)$< 3 \times 10^4$, which is 41% of the full sample, and L(2-10keV)/L(1.4 GHz)$< 10^3$ for 5 sources, i.e. 18% of the full sample. This difference between the expected and observed fraction of radio bright sources is not conclusive, because our radio fluxes may be over-estimated as discussed above. However, if we associate to the sources without a detection in the DR2 VLA-CDFS catalog the average flux measured above, the fractions of sources with L(2-10keV)/L(1.4 GHz)$< 3 \times 10^4$ and L(2-10keV)/L(1.4 GHz)$< 10^3$ are 92% and 19% respectively.

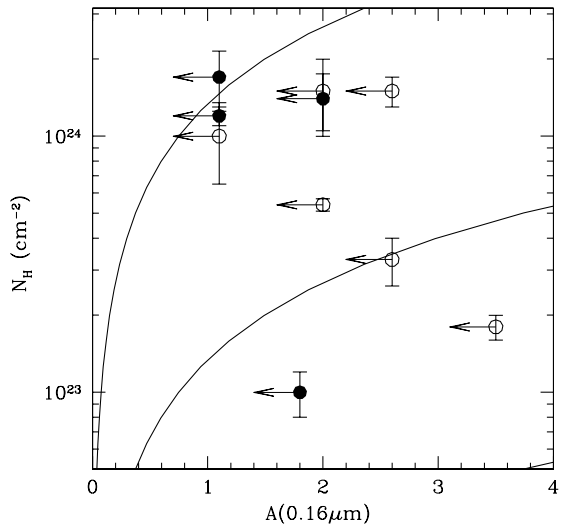

Fig. 3. The best fit N_H as a function of the 0.16μm extinction for the 10 z> 3 highly obscured or Compton thick AGN. Filled points are sources with point like optical or near infrared morphology. The two solid lines are the expectation for a dust-to-gas ratio 100 and 1000 times lower than the Galactic one.

We can therefore conclude that, at least on average, radio fluxes are higher than expected based on the X-ray fluxes and assuming common nuclear origin. If radio emission is dominated by stellar processes we can convert radio fluxes in star-formation rates (SFRs, see e.g. Yun et al. 2001). We used the following calibration which assumes a Chabrier IMF[2]:

$$SFR = 3.4 \times 10^{-22} L(1.4\mathrm{GHz}) \quad (2)$$

In two cases we have independent estimates of SFR, which agrees reasonably well with the values in Table 3. M208, has a SFR$\sim$ 1000M$_\odot$/yr estimated from a Laboca 870μm detection (see Gilli et al. 2011), while M4417 has SFR$\sim$ 440M$_\odot$/yr, estimated from UV SED fitting and oxygen lines (Maiolino et al. 2008).

3.2.1. A high-z star-forming galaxy?

Rather peculiar is the case of M4417, a galaxy studied by Maiolino et al. 2008 in the framework of the AMAZE program. The X-ray luminosity corresponding to the observed SFR is logL(2-10keV)$\sim$ 42.35 (by using the Ranalli et al. 2003 conversion factor), just a factor 40% lower than the observed X-ray luminosity. It should be noted that although the Chandra X-ray contours seems centered on M4417 (see Fig. 4), there could be some contribution to the observed X-ray flux from the nearby z=3.471 galaxy M4414, which has a SFR $\sim$ 1/4 that of M4417. Intriguingly, M4417 is the Chandra-GOODS-MUSIC and Chandra-GOODS-ERS object with the lowest X-ray to z band and H band flux ratios (0.004 and 0.005 respectively), lower than typical AGN (see next section), further suggesting that the X-ray emission from this object is not dominated by a nuclear source. We then conclude that the observed X-ray luminosity is likely dominated by stellar sources, making M4417 one of the farthest objects in which X-rays are probing stellar processes. Of course other solutions are possible, for example M4417 may be a reflection dominated, heavily Compton thick AGN, where the nucleus is completely hidden and the observed X-ray luminosity is just a fraction of the real one. We do not have however evidences in this direction from either X-ray colors, optical spectroscopy, infrared spectroscopy and broad band UV to infrared SED (the source is not detected at wavelengths longer than 8μm, see Fig. 4).

There are other two sources with relatively low X-ray luminosity and high radio flux: E2551 and E1516. In these cases the X-ray luminosity corresponding to the SFR rate estimated from the radio flux is a factor of 70% and 90% lower than the observed X-ray luminosity. Their X-ray to H band ratio are however $\gtrsim$10 times higher than that of M4417 (0.06 for E2551 and 0.07 for E1516). The radio flux and luminosity of E2551 are the highest in the sample, suggesting that this may well be a radio loud AGN.

3.3. X-ray to optical/NIR flux ratios and selection effects

The standard procedure to assemble X-ray high-z AGN samples is through the optical identification of X-ray source catalogs. We used in the previous section a complementary approach, that is studying the X-ray emission of optically or NIR selected high-z galaxies. In the first case the problem is to be sure that the optical/NIR identification of the X-ray source is correct, and that sample identifications are reasonably complete. In the latter case the problem is the reliability and completeness of the optical/NIR samples. They should include most of the galaxies (and therefore most AGN) down to a reasonably low flux limit. The GOODS-MUSIC catalog is fairly complete down to $z \sim 26$ and F(4.5μm)$\sim$ 1.5μJy and includes sources down to $z \sim 27$ and F(4.5μm)$\sim$ 0.5μJy. The GOODS-ERS catalog is fairly complete down to H$\sim$ 26.5 and includes sources down to H$\sim$ 27.5. To understand how these optical and NIR flux limits translate into X-ray flux limits we compute the X-ray (0.5-2keV) to NIR (H band) flux ratio F(0.5-2keV)/F(H) of much brighter, and therefore likely complete, AGN samples. Fig. 5 compares F(0.5-2keV)/F(H) of the z> 3 Chandra-GOODS-ERS and Chandra-GOODS-MUSIC AGN samples to the Chandra-COSMOS (Civano et al. 2011) and XMM-COSMOS (Brusa et al. 2009a, Brusa et al. 2010) z> 3 AGN samples. The COSMOS samples are X-ray selected samples with nearly complete optical identification, thanks to the fact that they cover X-ray and optical/NIR flux ranges 10-100 times brighter than the Chandra-GOODS-ERS and Chandra-GOODS-MUSIC AGN samples, and the massive photometric campaigns performed in this field with HST/ACS, Subaru and CFHT (Capak et al. 2008). As an example, there are only two sources in the Chandra-COSMOS catalog without an optical or infrared counterpart, 19 without an optical counterpart, 0.1% and 1% of all Chandra-COSMOS sources respectively, Civano et al. 2011. Most of these sources are likely high luminosity highly obscured type 2 QSOs (e.g. Fiore et al. 2003). But even assuming that *all* these 19 sources are at high-z, they would be 25% of the z> 3 sources in Chandra-COSMOS. So this is a very conservative upper limit to the Chandra-COSMOS completeness at high-z. Similar numbers apply to the XMM-COSMOS survey.

[2] assuming a Salpeter IMF would result in SFR $\sim$ 1.7 times higher

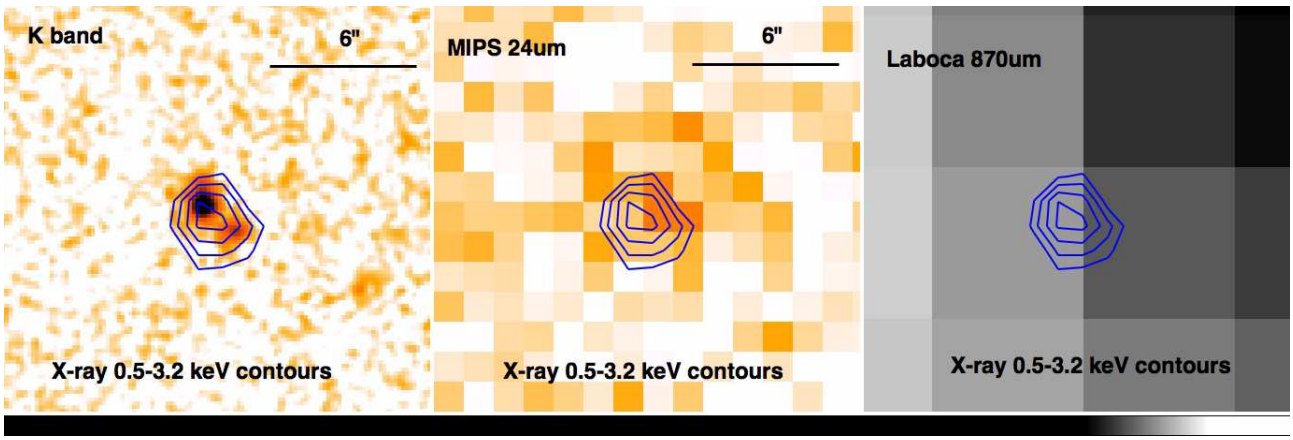

Fig. 4. K band, MIPS 24μm and LABOCA 870μm images around the M4417 galaxy with overlaid X-ray 0.5-3.2 keV contours.

The Chandra-GOODS-ERS detections cover a range of F(0.5-2keV)/F(H) similar to the COSMOS samples and indeed the Chandra-GOODS-ERS and COSMOS distributions of F(0.5-2keV)/F(H) are perfectly consistent (the probability that the Chandra-GOODS-ERS and Chandra-COSMOS distributions are drawn from the same parent population is 50%, using the Kolmogorov-Smirnov test). This suggest that the HST/WFC3 ERS H band images are deep enough to trace high-z AGN populations at the extremely faint X-ray flux limits reached by the Chandra 4 Msec exposure, avoiding significant incompleteness, or at least with an incompleteness comparable to that reached at much brighter fluxes by Chandra-COSMOS and XMM-COSMOS. The same exercise performed using the GOODS-MUSIC z band and IRAC 4.5μm selected catalog is not satisfactorily (we used to this purpose a subsample of the full Chandra-GOODS-MUSIC sample with deep H band VLT/ISAAC coverage, excluding 13 sources with shallower H band coverage). The Chandra-GOODS-MUSIC sample clearly misses sources with high F(0.5-2keV)/F(H) flux ratio in comparison to the Chandra-GOODS-ERS and COSMOS samples, and indeed the Chandra-GOODS-MUSIC F(0.5-2keV)/F(H) distribution is inconsistent with the Chandra-COSMOS distribution at the 99.925 % confidence level (using the Kolmogorov Smirnov test). This means that the GOODS ACS and IRAC images are not deep enough to fully probe the AGN population at the flux limits of the CDFS 4 Msec observation. The F(0.5-2keV)/F(H) distribution of the Chandra-GOODS-MUSIC sources with F(0.5-2keV)$\gtrsim 5\times10^{-17}$ erg/cm^2/s is consistent with the GOODS-ERS and COSMOS ones (probability of $\sim$ 30% that they can be drawn from the same parent population) and therefore in the following we will consider only the 23 Chandra-GOODS-MUSIC sources brighter than this flux limit (and outside the ERS area). These 23 sources are added to the 17 sources of Chandra-GOODS-ERS sample to form a total sample of 40 high-z AGN. We use this sample to constrain the faint end of the AGN luminosity function at high redshift.

4. High-z AGN luminosity functions

Our z$>$ 3 AGN candidate sample includes 17 Chandra-GOODS-ERS sources and 23 Chandra-GOODS-MUSIC sources spanning a range in luminosity 42.5$<$logL(2-10keV)/ergs/s$<$44.8. They can be used to probe the faint end of the high-z AGN luminosity functions. We calculated the comoving space densities of our high-z sample using the $1/V_{max}$ method (Schmidt 1968). We choose L(2-10keV) and z ranges to ensure completeness at the X-ray flux limit F(0.5-2keV)$\sim 2\times10^{-17}$ erg/cm^2/s reached by our survey. The luminosity limit at z=4, 5 and 7.5 is logL(2-10keV)$\sim$ 42.7, 42.8, 43.3 respectively. Accordingly we compute comoving space density in the redshift bins 3-4, 4-5 and 5.8-7.5 with luminosity ranges 42.75-44.5, 43-44 and 43.5-44.5 respectively. There are a total of 30 Chandra-GOODS-ERS and Chandra-GOODS-MUSIC AGN in these redshift and luminosity bins. Comoving space densities are given in Table 4. Fig. 7 presents the AGN luminosity functions in the same redshift bins. Errors are computed using Poisson statistics on the number of AGN in each redshift-luminosity bin. To obtain information on the slope of the luminosity functions we joined the above samples with the Chandra-COSMOS high-z sample of Civano et al. 2011, the XMM-COSMOS sample of Brusa et al. 2009a, the GOODS sample of Fontanot et al. 2007, the faint optical AGN sample of Glikman et al. 2011, the luminous optical AGN samples of Richards et al. 2006 and Jiang et al. 2009. We converted the rest frame 1450 Å luminosities of the optically selected samples to the 2-10 keV band using the Marconi et al. 2004 and Sirigu et al. 2011 luminosity dependent conversion factors. We assume no intrinsic reddening in the optically selected, high-z AGN. This might underestimate the real AGN luminosity, if significant dust is present along the high-z AGN lines of sight (Maiolino et al. 2004, Jiang et al. 2006, Gallerani et al. 2010). We checked our conversion factors against real data, using the Chandra and XMM detections of the Jiang et al. 2009 QSOs (Mathur et al. 2002, Shemmer et al. 2006 and references therein). Fig. 6 shows the ratio between the UV 1450Å luminosity and the 2-10 keV luminosity against 1450Å luminosity for 12 QSOs at z$>$ 5.7 for which we collected X-ray data from the literature. The figure also shows the UV to X-ray conversion adopted in this work, which agrees quite well with the data of this high redshift QSO sample.

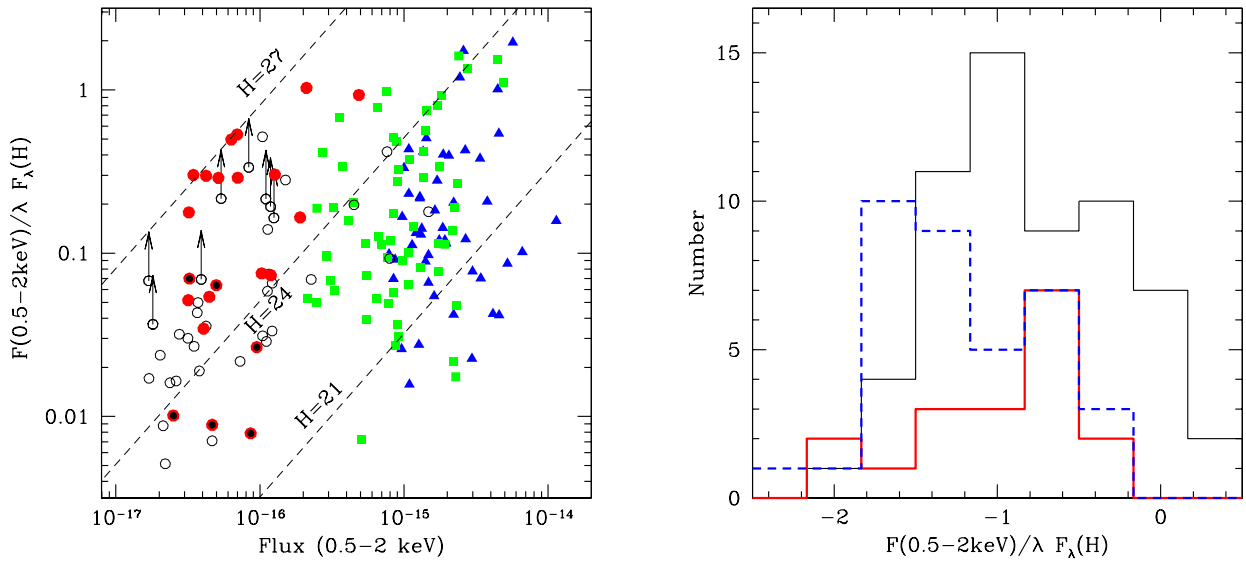

Fig. 5. [Left panel]: The X-ray to NIR flux ratio F(0.5-2keV)/F(H) as a function of the X-ray flux for the z> 3 Chandra-GOODS-ERS AGN sample (red-filled circles), Chandra-GOODS-MUSIC sample (black-open circles), Chandra-COSMOS sample (green-filled squares) and XMM-COSMOS sample (blue-filled triangles. [Right panel:] The distributions of F(0.5-2keV)/F(H) for the Chandra-COSMOS z> 3 sample (black histogram), Chandra-ERSVO sample (red histogram), and Chandra-GOODS-MUSIC sample (blue, dashed histogram).

Table 4. Chandra-GOODS-ERS z>3 AGN comoving space densities

logL(2-10keV)	3-4	4-5	3.8-5.2	5.8-7.5
42.75-43.5	$4.3^{+2.9}_{-1.9} \times 10^{-5}$	–	–	
43.5-44.0	$4.0^{+1.7}_{-1.2} \times 10^{-5}$	–	–	
44.0-44.5	$1.6^{+1.3}_{-0.8} \times 10^{-5}$	–	–	
43-44	–	$2.1^{+0.9}_{-0.7} \times 10^{-5}$	$3.5^{+1.9}_{-1.3} \times 10^{-5}$	
43.5-44.5	–	–	–	$0.66^{+1.1}_{-0.5} \times 10^{-5}$

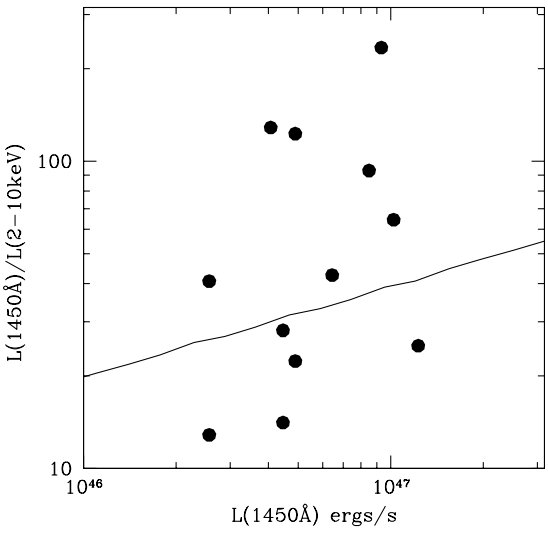

Fig. 6. The UV 1450Å to X-ray 2-10 keV luminosity ratio for 12 QSOs at z> 5.7

We modeled the wide luminosity range high-redshift luminosity functions using the standard double power law shape:

$$\frac{\mathrm{d}\Phi(L_\mathrm{X})}{\mathrm{dLog}L_\mathrm{X}} = A[(L_\mathrm{X}/L_*)^{\gamma 1} + (L_\mathrm{X}/L_*)^{\gamma 2}]^{-1}. \quad (3)$$

where A is the normalization factor for the AGN density, $\gamma 1$ and $\gamma 2$ are the faint-end and bright-end slopes and L_* is the characteristic break luminosity. Optical selection may miss highly obscured AGN, which can represent a large fraction of the total in particular at low luminosity (La Franca et al. 2005). To avoid possible incompleteness in optical surveys we excluded from the fit the optically selected AGN density determinations with $M_{1450} > -26.5$ (or correspondingly L(2-10keV)<45.1). We first fitted this simple model to the luminosity functions in the three redshift bins. The number of points in the z=3-4 redshift bin allows us to constrain all four parameters. This is not possible in the redshift bins 4-5 and > 5.8, where we fitted the data fixing the slopes $\gamma 1$ and $\gamma 2$ to the best fit values found in the z=3-4 redshift bin. The results of these fits are reported in Table 5. As a next step, we fitted simultaneously the data in the three redshift bins with an evolutionary model. We chose to describe the evolution of the high-z AGN luminosity function with the *LADE* (luminosity and density evolution) model, introduced by Aird et al. 2010. Thus the evolution of L_* is given by:

$$\mathrm{Log}L_*(z) = \mathrm{Log}L_0 + p\mathrm{Log}(1+z) \quad (4)$$

and the evolution of A is given by:

$$\mathrm{Log}A(z) = \mathrm{Log}A_0 + d\mathrm{Log}(1+z) \quad (5)$$

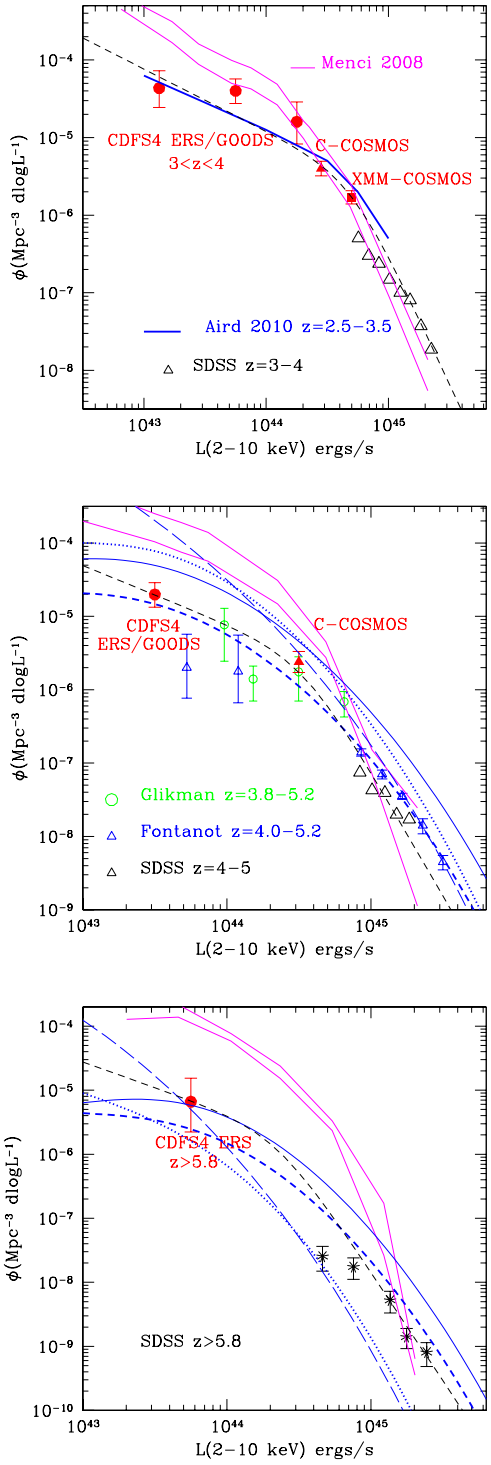

Fig. 7. The AGN 2-10 keV luminosity functions at z=3-4 (top panel), z=4-5 (central panel) and z>5.8 (bottom panel). Large red-filled circles are from the CDFS Chandra-GOODS-MUSIC and Chandra-GOODS-ERS samples. Red-filled triangles are from Chandra-COSMOS (Civano et al. 2011), red-filled squares from XMM-COSMOS (Brusa et al. 2010). The blue thick curve in the top panel is the LADE model of Aird et al. 2010 in the 2.5-3.5 redshift bin. Large black-open triangles are SDSS data from Richards et al. 2006, stars are SDSS data from Jiang et al. 2009, open circles are from Glikman et al. 2011 and small blue-open triangles are from Fontanot et al. 2007. Black dashed curves are best fits to the X-ray plus optical, wide luminosity range luminosity functions (see text for details). Magenta solid curves encompass predictions on the Menci et al. (2006, 2008) semi-analytic model. Blue curves are models from Shankar et al. (2011), see the Discussion for details.

We first fitted the data with the full six parameter model. The $\gamma1$ and $\gamma2$ slopes turned out similar to those obtained fitting the z=3-4 data only (the z=3-4 data provides the strongest constrain to the shape of the luminosity function). We report in Table 5 the best fit parameters obtained by fixing $\gamma2$ to 3.4 and to 3.0 (keeping the faint-end slope $\gamma1$ fixed at 0.8 in both cases). The fit with $\gamma2 = 3$ produces a χ^2 significantly worse than for the best fit case, but still acceptable considering the uncertainties on the correction between the optical and X-ray luminosities for the optically selected AGN density determinations. We found that the A_0 and d parameter are completely degenerate. We could obtain equally good fits with combinations of A_0 and d inversely correlated. We report in Table 5 the best fits obtained with $d = 0$ (no density evolution) and $d = -1$. On the other hand, the data are good enough to constrain relatively well L_0 and p. Our data are thus consistent with a pure luminosity evolution, with L_* rather quickly reducing with the redshift. The dashed lines on Fig. 7 are the best fit pure luminosity evolution model (4) in Table 5.

It is not straightforward to compare our high-z, wide luminosity band luminosity functions with previous determinations. The best fit model of Shankar et al. 2009a agrees quite well with our determinations at logL(2-10keV)< 44 but overestimate the density of higher luminosity AGN, in particular of optically selected AGN. It should be noted that that Shankar et al. 2009a adopt UV to X-ray luminosity conversion factor fixed at 10.4, while our conversion factor varies with the luminosity, from 4.4 at logL(2-10keV)=43 to 27 at logL(2-10keV)=45. Furthermore, Shankar et al. 2009a correct for extinction and the fraction of Compton thick AGN. As discussed above our data are not corrected for the fraction of Compton thick object, because several have actually been found in our samples, and we use optically selected AGN of high luminosity ($M_{1450} > -26.5$, L(2-10keV)<45.1), where the fraction of obscured AGN is likely to be small. Hopkins et al. 2007 use a luminosity dependent bolometric correction, but with a different calibration with respect to ours. They correct their data for extinction and the fraction of Compton thick AGN missed in optical, X-ray and infrared surveys. They convert N_H distributions evaluated from X-ray data into optical-UV reddening using a canonical gas-to-dust ratio, which, as discussed in the previous section (and by e.g. Maiolino et al. 2001, Shi et al. 2006), can overestimate the real extinction, in particular when the X-ray absorber is compact, smaller than the dust sublimation radius. They find z> 3 luminosity functions with much flatter slopes with respect to ours (or to the Shankar et al. 2009a ones). As an example, the Hopkins et al. 2007 best fit model would predict $\sim 2-4$ times more z=3-4 and z=4-5 AGN with logL(2-10keV)> 44.5 than actually found in the XMM and Chandra COSMOS surveys (Brusa et al. 2009a, Civano et al. 2011).

4.1. AGN luminosity function and duty cycle evolution

It is interesting to put the findings of the previous section in a context, to study the evolution of the AGN luminosity function from the local Universe to z$\sim$ 6. We compare in the upper panel of Fig. 8 the best fits to the z=3.5, z=4.5 and z=6 AGN luminosity functions (model 4 in Table 5) to the best fit model luminosity functions found at lower redshift by La Franca et al. 2005. These have been computed

Table 5. Modeling the high redshift AGN luminosity function

model	z range	A or A_0 10^{-6} Mpc^{-3}	L_* or L_0 10^{44} ergs/s	$\gamma 1$	$\gamma 2$	p	d	χ^2 (dof)
1	3-4	$3.0^{+4.9}_{-1.5}$	5.4 ± 2.2	0.8 ± 0.2	$3.4^{+0.6}_{-0.4}$	–	–	4.63 (4)
2	4-5	$3.2^{+1.2}_{-1.1}$	3.5 ± 0.4	0.8 FIX	3.4 FIX	–	–	2.52 (2)
3	> 5.8	$2.4^{+3.3}_{-2.0}$	$2.1^{+3.1}_{-0.5}$	0.8 FIX	3.4 FIX	–	–	1.23 (1)
4	> 3	$3.3^{+0.7}_{-1.0}$	120^{+60}_{-30}	0.8 FIX	3.4 FIX	-2.1 ± 0.2	0 FIX	10.65 (14)
5	> 3	$5.2^{+1.1}_{-1.6}$	130^{+70}_{-40}	0.8 FIX	3.0 FIX	-2.4 ± 0.2	0 FIX	16.09 (14)
6	> 3	$1.6^{+0.3}_{-0.5}$	70^{+30}_{-20}	0.8 FIX	3.4 FIX	-1.8 ± 0.2	-1 FIX	10.82 (14)
7	> 3	$2.6^{+0.6}_{-0.8}$	75^{+40}_{-25}	0.8 FIX	3.0 FIX	-2.03 ± 0.15	-1 FIX	15.77 (14)

by correcting for the incompleteness due to X-ray absorption, which is important at low redshift where the photoelectric cut-off produced by the typical column densities observed in many AGN is well within the X-ray selection band. The La Franca et al. 2005 luminosity functions are consistent with the new determinations of Aird et al. 2010 and Ebrero et al. 2009, based on a larger number of objects. The upper panel of Fig. 8 summarizes the complex evolution of the AGN luminosity function, which rises from z=0 up to z=1, 2, 3 for increasing luminosities and than decreases at higher redshifts.

We converted these luminosity functions into "active" SMBH mass functions by using MonteCarlo realizations. We simulated 10^8 AGN luminosities and SMBH masses in each redshift bin according to the following procedure. 1) We first randomly choose an X-ray luminosity following the luminosity function distribution in each given redshift bin; 2) we than convert it into a bolometric luminosity using the Marconi et al. 2004 and Sirigu et al. 2011 luminosity dependent bolometric correction; 3) we randomly choose an Eddington ratio from given distributions. We used log-normal distributions with parameters in Table 6. At z$<$ 0.3 we used the distribution of Netzer 2009b, which are shifted toward higher Eddington ratios with respect to the Kauffmann & Heckman 2009 distributions (see the discussion in Netzer 2009b, Netzer 2009a). At medium to high redshift we used the distributions of Trakhtenbrot et al. 2011, Shemmer et al. 2004, Netzer & Trakhtenbrot 2007, Willott et al. 2010b. This provides a SMBH mass for each chosen X-ray luminosity and Eddington ratio. 4) We finally binned the resulting SMBH distributions in each redshift bin to build SMBH mass functions. The resulting "active" SMBH mass functions in six redshift bins are plotted in the central panel of Fig 8. It must be stressed that this is an empirical calculation, performed independently in each redshift bins, using only observed quantities. It does not pretend to model the history of SMBH growth through the cosmic times, which can be obtained by using a continuity equation, conserving the number, as in Marconi et al. 2004, Merloni & Heinz 2008, Shankar et al. 2009a.

Furthermore, the adopted Eddington ratio distributions all refer to relatively luminous AGN. Less active SMBH, giving rise to low luminosity AGN and LINERs are not represented in these distributions. For this reason we adopted a luminosity limit for the computed SMBH mass functions: these functions represent "active" SMBH producing an X-ray luminosity $> 10^{43}$ ergs/s. As a consequence, comparison with previous calculation is not straightforward. For example, while our SMBH mass functions are luminosity limited, the "active" SMBH mass functions of Merloni & Heinz 2008 are X-ray flux limited mass functions. The 2-10 luminosity corresponding to the faintest flux limit of Merloni & Heinz 2008 is $\sim 10^{40}$ ergs/s at z=0.1, $\sim 10^{43.1}$ and $\sim 10^{43.5}$ at z=3, while we plot the SMBH mass function of AGN more luminous than $\sim 10^{43}$ in all redshift bins. SMBH mass functions of broad line AGN have been computed by Kelly et al. 2010, by using about 10.000 SDSS QSOs in the redshift range 1–4.5. Our SMBH mass functions are consistent, or slightly higher than the Kelly et al. determinations at most redshifts and black hole masses considered, as expected since broad lines AGN are a fraction of the full active SMBH population, even at the highest SMBH masses and/or AGN luminosities. The only regime where our estimates are significantly higher than the Kelly et al. ones are the highest masses (logM$>$ 9.3M$_\odot$) at z$\sim$ 1, where the Kelly et al. 2010 function drops steeply, while our function decreases more smoothly.

The SMBH mass functions can be transformed into stellar mass function of "active" galaxies by assuming a conversion factor between SMBH mass and host galaxy stellar mass. We assumed a mean value $\Gamma_0 = log(M_{BH}/M_*) = -2.8$ at z$\sim$ 0 (Haring & Rix 2004 but also see the discussion in Lamastra et al. 2010) and a redshift evolution $\Gamma \sim \Gamma_0 \times (1+z)^{0.5}$ (Merloni et al. 2004, Hopkins et al. 2006, Shankar 2009). It should be noted that in the local Universe the above correlation has been found and calibrated for the bulge component of galaxies. Whether a strict distinction between bulge and disk still exist at high-z is a matter of debate. Disks of z$\sim$ 2 galaxies are much more compact and much thicker that in today spirals of similar mass (Genzel et al. 2006, van der Wel et al. 2011). For the sake of simplicity we assume in the following calculation that the SMBH mass is proportional to half of the total stellar mass of high-z galaxies. It is instructive to compare the SMBH mass functions and the "active" galaxies stellar mass functions to the stellar mass functions of all galaxies. The lower panel of Fig. 8 plots a collections of galaxy stellar mass functions: we used the stellar mass functions of Fontana et al. 2006 at z$\lesssim$2, Santini et al. 2011 at z=3-4, Caputi et al. 2011 at z=4-5 and Stark et al. 2009 at z=6.

The AGN fraction, or AGN duty cycle, can finally be obtained by dividing the "active" galaxy stellar mass functions by the galaxy stellar mass functions. Following the adopted luminosity limit used to compute SMBH mass functions, we define AGN duty cycle the fraction of AGN with 2-10 keV luminosity greater than 10^{43} ergs/s to the total number of galaxies with a given stellar mass. Lower luminosity AGN do exist and are probed by the luminosity functions in Fig. 8 up to z$\sim 2-3$. However, they are below the flux limit of current surveys at higher redshift. Therefore, our luminosity threshold also avoids problems of

Table 6. Parameters of log-normal Eddington ratio distributions

z	peak	width dex
0-0.3	0.03	0.5
0.3-1	0.1	0.33
1.5-2.5	0.18	0.33
3-4	0.22	0.33
4-5	0.5	0.33
> 5.8	1.0	0.25

incompleteness of the samples at high-z. According to this definition, the AGN duty cycle can be different from the AGN timescale, since the latter is correlated with the total inntrinsic lifetime of the AGN, which can include phases with luminosity $< 10^{43}$ ergs/s. The AGN duty cycle is plotted in the upper panel of Fig. 9. It must be stressed again that this is an empirical calculation, performed independently in each redshift bin, using only the observed AGN and galaxy luminosity and mass functions and observed Eddington ratio distributions. We find that the AGN duty cycle increases at all redshift with the stellar mass. Similar trends have been found by Kauffmann et al. 2003, Best et al. 2005, Bundy et al. 2008, Yamada et al. 2009, Brusa et al. 2009b for optically selected, radio selected and X-ray selected AGN. At each given stellar mass the duty cycle increases with the redshift up to z=4-5, consistent with the result of Marconi et al. 2004, Brusa et al. 2009b, Shankar et al. 2009a. There are 22 galaxies in the GOODS-ERS catalog with z$>$ 3 and stellar mass higher than $10^{11.25}$ $M_{\odot}$, 7 of which are X-ray sources in Table 1, thus confirming an AGN duty cycle $\gtrsim$30% at z$>$3 for such massive galaxies. Fig. 9, lower panel, plots the evolution of the AGN duty cycle as a function of the redshift for two galaxy stellar masses: log(M_s)=11.25 and 11.75. Bands are plotted rather than curves to emphasize the rather large uncertainties, especially at high-z (see next section). The same Fig. shows previous evaluations by Brusa et al. 2009b. These are consistent with the present estimates within their rather large error bars. The expectations of the Menci et al. 2008 semi-analytic model are also showed in the lower panel of Fig. 9.

4.1.1. Error budgets

The determination of the evolution of the AGN duty cycle is plagued by large uncertainties, especially at high redshifts. It is therefore important to study in detail the origin of these uncertainties and the way of reducing them.

The uncertainty on both the AGN comoving densities at z$<$2 (at least for unobscured and moderately obscured AGN) and on the stellar mass functions at z$<$ 2 are relatively small, of the order of 10-20% or even smaller, thanks to large AGN and galaxy samples used for these determinations and thanks to the use of several different surveys, which helps in reducing the systematic error. The largest uncertainty in the AGN luminosity function is on the fraction of Compton thick AGN. The fraction of these objects in the local Universe is high: 30-50% of the optically selected Seyfert 2 galaxies can be Compton thick ($\approx$ 1/4 − 1/3 of the full AGN population, Risaliti et al. 1999, Panessa et al. 2006, a result confirmed by hard X-ray selection, see Malizia et al. 2009).

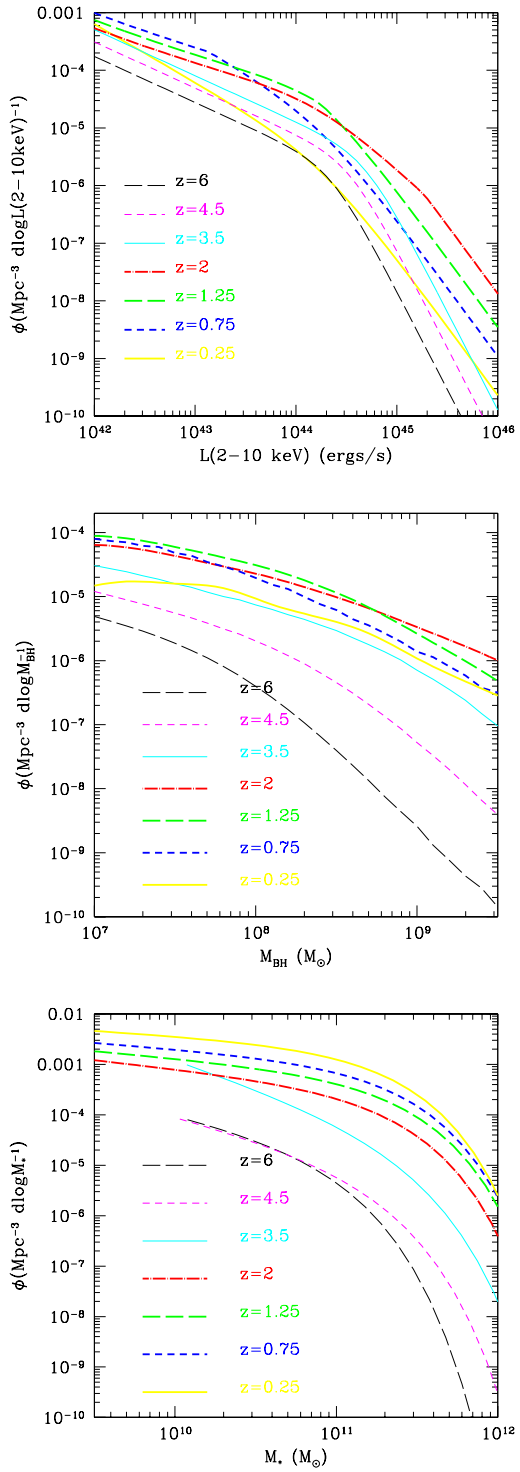

Fig. 8. [Top panel:] A collection of AGN luminosity functions. z$\lesssim$2 from La Franca et al. 2005, z$>$ 3 this work. [Central panel:] SMBH mass functions obtained by combining the AGN luminosity functions in the top panel with Eddington ratio distributions (see the text for details). [Bottom panel:] A collection of galaxy stellar mass functions. z$\lesssim$2 from Fontana et al. 2006, z=3-4 from Santini et al. 2011, z=4-5 from Caputi et al. 2011, z=6 from Stark et al. 2009.

At higher redshift the fraction of Compton thick AGN

is more uncertain but it can be as high as 1/3 of the full AGN population (Fiore et al. 2008, Fiore et al. 2009), or even higher (Daddi et al. 2007, Treister et al. 2010). A fraction of Compton thick sources $\sim 1/3$ of the total is actually included in the model of La Franca et al. 2005, and therefore we are confident that the error on the total AGN comoving space density at z< 2 due to undetected, and unaccounted for, Compton thick sources is small ($\lesssim 10-20\%$)

At z> 3 the uncertainties on both AGN luminosity function and galaxy mass functions are larger, in particular at low AGN luminosities and low galaxy masses (see Table 3), they are of the order of 30-50% at z=3-5. At z$\sim$ 6 the uncertainties on the faint end of the AGN luminosity function and on the galaxy stellar mass function are extremely large, a factor 100%. These uncertainties are dominated by statistics in the case of AGN (only few detections at z>4-5) and by systematics in the case of the galaxy mass function (at z$\sim$ 6 stellar masses are estimated by Stark et al. 2009 by converting the UV luminosity into stellar mass, which is a highly uncertain procedure). The uncertainty due to undetected or unaccounted for Compton thick AGN at z> 3 is smaller than the above features. In fact, we note that at z> 3 the cut-off produced by a column density 10^{24} cm^{-2} is shifted below 2.5 keV, where the effective area of Chandra and XMM peaks. This, together with the extremely deep exposures of the CDFS, helps in detecting directly at least mildly Compton thick sources (Georgantopoulos et al. 2009, Georgantopoulos et al. 2011, Feruglio et al. 2011, Gilli et al. 2011, Comastri et al. 2011). Indeed, about one fifth of the Chandra-GOODS-ERS sources can be Compton thick, as well as one fourth of the Chandra-GOODS-MUSIC sources with optical spectroscopy (see Sect. 3.2), and many are directly detected in our z>3 search. We are therefore confident that the uncertainty on the total AGN comoving density linked to Compton thick AGN is at most $\sim 10-20\%$ also at z> 3. The high luminosity end of our z>3 luminosity functions is probed by optical surveys. Obscured AGN may well be missed in these surveys, and therefore these determinations may be regarded as lower limits. We note, however, that the fraction of obscured AGN decreases strongly with the luminosity (at least at z< $2-3$ where large area X-ray surveys provided samples of high luminosity QSOs), and therefore the error on the comoving space density of high luminosity AGN at z> 3 is also likely to be small (< 20%). We should consider the uncertainty in the conversion from UV to X-ray luminosities for the optically selected AGN luminosity functions. This uncertainty is probably of the order of 30% (see the discussion in Shankar et al. 2009a).

Another relatively large source of error in the evaluation of the AGN duty cycle is represented by the uncertainty on the Eddington ratio distributions. We performed several tests using parameters slightly different than those in Table 4. For these AGN we found that the duty cycle (at logM_*=11) changes by a factor of 15-30% and $\sim$ 100% for distribution peak and width differing by 30% from the assumed ones. The biggest effect is introduced by the width of the Eddington ratio distributions: the broader the distribution the higher is the resulting AGN duty cycle. The uncertainty on the Eddington ratios is particularly severe for low luminosity, logL(2-10keV)< 43 AGN. Since this is also, roughly, the luminosity limit of our z> 3 sample, we decided to limit the analysis to AGN with logL(2-10keV)> 43 ergs/s only, and assume conservatively a 50% (total) relative error on the AGN duty cycle arising from the uncertainty on Eddington ratios.

Finally, we adopted given normalization and evolution of the SMBH to galaxy stellar mass ratio Γ and assumed that is is the same for each object at each given redshift. However, we know that, at least at low redshift, the SMBH-bulge mass relation is unlikely to be universal (Mathur et al. 2001, Mathur et al. 2011 and references therein). Furthermore, Batcheldor 2010 suggest that selection effects are important in shaping the SMBH-bulge mass relation. Thus, the deviations in the SMBH mass-bulge mass relations resulting from galaxy morphology, orientation and selection effects can affect the duty cycle calculations, in particular at small masses. We assumed a redshift evolution $(1+z)^{0.5}$, consistent with our present knowledge and with the expectation of several models Lamastra et al. 2010, Hopkins et al. 2006, Shankar et al. 2009a. However, the uncertainty on this calibration increases with the redshift, and can be rather large at z> $3-4$. To quantify all these effects is not an easy task. As an example, if Γ is half of what assumed above, the duty cycle is reduced by a factor between 20% and 100%, depending on the galaxy stellar mass and redshift. In summary, the bands plotted in Fig. 9 roughly account for the typical errors given above at each given redshifts and galaxy stellar masses.

5. Discussion

We evaluated the comoving space density of the z> 3 faint X-ray sources in three redshift bins: 3-4, 4-5 and > 5.8. The number of AGN in the three redshift bins is small, 19, 9 and 2 respectively, and therefore we were forced to use relatively wide luminosity bins, to keep the statistical error reasonably small. In particular, the comoving space density at z> 5.8 and logL(2-10keV)=43.5-44.5 has been computed using only two sources. We stress that in one case a secondary solution in the photometric redshift does exist at z$\sim$ 2, so our determination is probably an upper limit to the true space density of low luminosity AGN at > 5.8. This confirms that the slope of the faint end of the z> 5.8 AGN luminosity function is significantly flatter than the bright end slope (see e.g. Shankar & Mathur 2007). We also note that the other claimed z> 7 AGN in the CDFS (L306, M70437), has a 0.5-2 keV flux below our threshold for Chandra-GOODS-MUSIC sources, and that the photometric solution of GOODS-MUSIC is broader than Luo et al. 2010 one, with a lower limit at z=2.7. This source is therefore *not* part of the > 5.8 sample used in Fig. 7. Recently Treister et al. 2011 evaluated the integrated AGN emissivity at z$\sim$ 6 by stacking together the CDFS and CDFN X-ray data at the position of the z$\sim$ 6 Bouwens et al. 2006 galaxy candidates. They obtained a luminosity density of 1.6×10^{46} ergs/s/deg^2 in the 2-10 keV band. If we integrate our z$\sim$ 6 best fit model above logL_X=42 we obtain a total luminosity density of 7.5×10^{38} ergs/s/Mpc^3 or 5.6×10^{45} ergs/s/deg^2, a value $\sim$ 2.8 times smaller than that reported by Treister et al. 2011. It must be noted that our determination is based on a fit to the broad luminosity range luminosity function obtained by joining single X-ray detections in the CDFS to the UV luminosity functions, while the Treister et al. 2011 is based

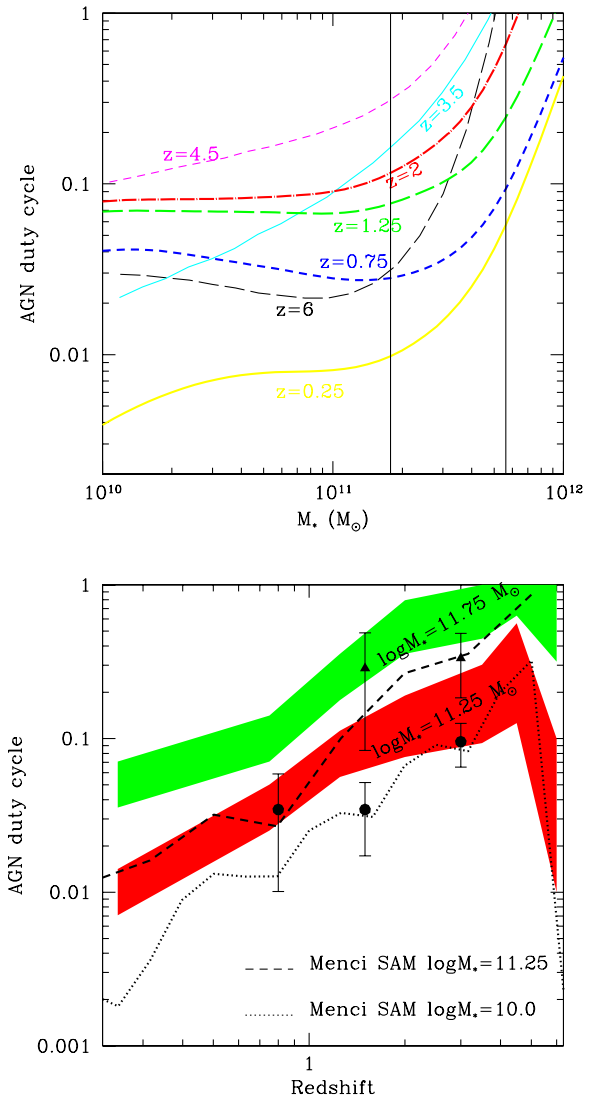

Fig. 9. [Top panel:] the AGN duty cycle as a function of the galaxy stellar mass in six redshift bins. AGN with logL(2-10keV)> 43 are considered only. [Bottom panel:] the AGN duty cycle as a function of the redshift for two galaxy stellar masses (logM_*=11.25, 11.75 $M_\odot$). Filled circles and triangles are previous determination by Brusa et al. 2009 for the same masses. The black dashed (dotted) curve is the expectation of the Menci et al.(2006,2008) SAM for logM_*=11.25 $M_\odot$ (logM_*=10 $M_\odot$).

on a stacking analysis of faint X-ray sources in both CDFS and CDFN.

Our results put some first constraints on the faint end of the AGN luminosity function (42.75<logL(2-10keV)<44.5) at z= 3 − 7, which are already interesting to be compared to model predictions. To constrain the shape of the AGN luminosity function we joined our determinations with those obtained at higher luminosities by shallower X-ray surveys (Chandra-COSMOS, XMM-COSMOS), and optical surveys (SDSS, NOAO DWFS/DLS). We then compared the broad luminosity range luminosity functions with the prediction of the semi-analytic model (SAM) of Menci et al. 2006, Menci et al. 2008. In this model baryonic processes are associated with the merging histories of dark matter (DM) haloes. These haloes contain hot gas at virial temperature, a fraction of which can radiatively cool down and form a disk with radius r_d and circular velocity v_d. During mergers, and also looser galaxy encounters (Cavaliere & Vittorini 2000), cold gas can loose its angular momentum and can be accreted by the nucleus. A fraction of this gas fuels a nuclear starburst while the rest can accrete on a central SMBH, giving rise to an AGN. The AGN timescale is $\tau \approx r_d/v_d$, i.e. the crossing time for the destabilized gas. Assuming typical values r_d ≈a few kpc and $v_d \approx$ 100 km/s the AGN timescale is short, a few 10^7 yr, comparable with the Salpeter timescale. In this SAM the AGN timescale, as well as AGN SMBH masses and Eddington ratios, are *not* free parameters, but are calculated self-consistently (the model only assumes that the accretion can proceed at most at the Eddington limit). The SAM includes a rather detailed treatment of AGN 'quasar mode' feedback (Menci et al. 2008), in terms of a blast wave carrying outwards the AGN power (Lapi et al. 2005). The SAM produces prediction for all AGN, both unobscured, moderately obscured and Compton thick. Lamastra et al. 2010 compares the SMBH masses and stellar masses of AGN host galaxies predicted by this SAM with measurements for various galaxy and AGN samples at different redshifts. This SAM reproduced reasonably well the z=3-4 luminosity function at logL(2-10keV)> 43.5. At lower luminosities it predicts 2-3 times more AGN than observed. It should however be noted that some extreme Compton thick AGN, those in which the nuclear emission is completely blocked by photoelectric absorption and Compton scattering, leaving only reflection emission in the X-ray band, can well be missed even in the deepest X-ray surveys. The agreement is sufficiently good at high luminosities (logL(2-10keV)> 45) at z=4-5 and z> 5.8 too. In these redshift bins the agreement between data and model gets worse at lower luminosities, where the Menci et al. 2008 SAM predicts 5-10 times more low luminosity AGN than in our determination and 2-3 times more than the Treister et al. 2011 ones.

To investigate the origin of this behaviour and get insights on high-z AGN physics we also compared our measurements with predictions derived from more basic models for AGN activation through galaxy interactions. This class of models consists of two ingredients: a DM halo merger rate compatible with cosmological simulations, and an input AGN light curve (e.g., Wyithe & Loeb 2003, Lapi et al. 2006, Shen 2009, Shankar 2009, 2010, and references therein). The initial mass of the SMBH at triggering is assumed to be a fixed small fraction of its mass at the peak of activity. SMBH growth is regulated by a condition between the peak luminosity and the mass of the host halo at triggering, consistent with the local relations between SMBHs and their host galaxies. The main advantage of approaching AGN modeling through this simplified technique is that not being part of a specific SAM, they can explore easily and quickly a large space of parameters and physical recipes to trigger AGN. Here we follow the models presented in the preliminary work by Shankar (2010a) with same parameters as in Shen (2009). A more comprehensive and detailed analysis of AGN merger models, with implications for SMBH scaling relations and AGN clustering (Shankar et al. 2010a,b) is beyond the scope of the present paper and will be discussed elsewhere (Shankar et al. 2011, in preparation). In this model AGN are activated by mergers of the

host DM haloes (ξ =M_{h2}/M_{h1} > 0.3 for major mergers, ξ > 0.1 includes minor mergers too). The AGN is triggered with no dynamical friction time delay between host halo and actual galaxy-galaxy merging (a solution close to the fly-by hypothesis of Cavaliere & Vittorini 2000). Super-Eddington accretion ($L/L_{Edd} = 3$) is allowed in the initial phases of BH growth, and a long, sub-Eddington post-peak phase is present in each event. Finally, a minimum halo mass M_{hmin} is assumed (see Shen 2009 for details). We plot in the central and lower panel of Fig. 7 four different models:

1. $\xi > 0.3$, $L/L_{\rm Edd} = 3$, $M_{hmin} = 3 \times 10^{11}\, M_{\odot}/h$ (blue, solid lines, reference model);
2. $\xi > 0.1$, $L/L_{\rm Edd} = 1$, $M_{hmin} = 3 \times 10^{11}\, M_{\odot}/h$ (blue, dotted lines);
3. $\xi > 0.3$, $L/L_{\rm Edd} = 3$, $M_{hmin} = 3 \times 10^{11}\, M_{\odot}/h$, without descending phase (blue, thick dashed lines);
4. $\xi > 0.3$, $L/L_{\rm Edd} = 1$, $M_{hmin} = 0.1 \times 10^{11}\, M_{\odot}/h$ (blue, long-dashed lines);

The purpose of the comparison of these models with the data is to understand whether the merger scenario produces expectations in agreement with the data and to highlight which of the underlying physical assumptions makes this match actually possible.

The reference model (1) overpredicts by a factor of 2-3 the AGN luminosity functions at z>4 at all luminosities but logL(2-10keV)=43.5-44.5 at z> 5.8. The same model without a descending phase (3) reproduces relatively well both the z=4-5 and the z> 5.8 luminosity functions. This suggests that the underlying AGN light curve must not be too prolonged in order not to generate too numerous faint, sub-Eddington AGN.

The inclusion of minor mergers steepens the AGN luminosity function at both z=4-5 and z> 5.8. Model (2) with $\xi > 0.1$ and $L/L_{Edd} = 1$ is roughly consistent with the z=4-5 luminosity function but underpredicts the bright end of the z> 5.8 luminosity function.

Relaxing the assumption of a minimum halo mass steepens again the AGN luminosity function at both z=4-5 and z> 5.8. The same model with $L/L_{Edd} = 1$ (model 4) overpredicts the low luminosity end of the z=4-5 luminosity function and underpredicts the high luminosity end of the z> 5.8 luminosity functions.

In conclusion, we find that the inclusion of minor mergers and the exclusion of a minimum halo mass both steepen the model luminosity function. About the first, minor mergers and galaxy fly-by helps the formation of stars at early times in the progenitors of today massive galaxies, thus helping in explaining their observed colors (e.g. Menci et al. 2004). They also help in reproducing quite well the X-ray AGN space densities at $z \lesssim 3$ (Menci et al. 2008). About the latter, there could be several causes for a minimum halo mass and/or for inefficiency of BH formation and growth in low mass halos. For example, in the SMBH formation scenario where seed BHs are formed from the monolithic collaps of gas clouds, the probability for a DM halo of hosting a BH seed is an increasing function of the halo mass (Volonteri et al. 2008). On the other hand, in the SMBH scenario where BH seeds are formed from PopIII stars, basically all DM halos with $M_h > 10^{9-10}$ $M_{\odot}$ at z< 7 are populated with BHs. Therefore, at least in principle, the faint end of the high-z AGN luminosity function might be used to discriminate among these two scenarios. However, there are at least other three effects that produce a minimum halo mass for BH formation and growth. First, the gravitational recoil, giving rise to ejection of one of the BH after a merging, can be more important at low masses (see e.g. Volonteri et al. 2011). Second, a cut-off in the build up of galaxies in haloes with $M_h < 10^{11}$ $M_{\odot}$ could be produced by a metallicity effect (Krumholz & Dekel 2011). Third, an intrinsic cut-off at low halo masses can be due to a cut-off in the primordial power spectrum of gravitational perturbation at small scales. Free streaming of *warm* DM leeds to a suppression on scales smaller than the free streaming scale and therefore to a cut-off. *Warm* DM has often been invoked to solve problems of the standard ΛCDM scenarios at small scales, such as the large number of galactic satellites, the cuspiness of galactic cores, and the large number of small, compact galaxies predicted by these models (see e.g. Primack 2009). However, the limits on the cut-off scale (or, equivalently, on the mass of the *warm* DM particle) derived from high-z Lyα forest are quite stringent: up to $\sim$ 100 kpc no cut-off is seen (Viel et al. 2008 and references therein). It is difficult to asses quantitatively which are the DM halo scales influenced by these effect. To this purpose we should include in our SAM and model both gravitational recoil and *warm* DM, and compare their prediction with AGN and galaxy luminosity functions. This is beyond the scope of this work and will be part of a separate publication (Menci et al. 2011, in preparation). A minimum halo mass for black hole growth implies that accretion is inhibited in halos smaller than this threshold mass (3×10^{11} $M_{\odot}$ in our models). BH seeds in these halos do not grow, until they are merged to BH in bigger halos. As a consequence, nuclear accretion occurs only on a fraction of the merging history, and the halo population when the above threshold is reached late will host SMBH with small masses. Qualitatively, they will be somewhat below the *Magorrian* correlation. Again, to obtain quantitative estimates we need to study the predictions of models including physical causes for the cut-off in the halo mass, which will be addressed in a forthcoming pubblication.

Finally, we have joined our present determination of the high-z AGN luminosity function with previous determination at lower redshift and with galaxy mass function determinations, to empirically estimate the AGN fraction (or AGN duty cycle), as a function of the galaxy stellar mass and redshift. We find that the AGN duty cycle increases with both host galaxy stellar mass and redshift. The AGN duty cycle is computed by assuming a given evolution of the *Magorrian* relationship. and by assuming distributions of Eddington ratios at different redshifts (see Table 6). These are far to be accurately known. Indeed the distributions of Table 6 taken from Trakhtenbrot et al. 2011, Shemmer et al. 2004, Netzer & Trakhtenbrot 2007, Willott et al. 2010b show an evolution with the redshift, while this is not the case for the distributions of Kollmeier et al. 2006. However, the increase of AGN duty cycle with redshift depends marginally on the evolution of the Eddington ratio, reflecting more basic AGN population properties, evidenced by the large evolution of the AGN number density (see e.g. Menci et al. 2006, Menci et al. 2008, Shankar et al. 2009b and references therein). The correlation of AGN duty cycle with both stellar mass and redshift is a rather robust result. It holds also by changing the calibration adopted for

the *Magorrian* relationship by a factor of 2. Our calculation confirms what clustering measurements suggest (e.g., Shankar et al. 2010a): the large clustering signal from luminous quasars implies that BHs reside in massive haloes that by definition are rare and thus require high duty cycles.

We compare in Fig. 9 the evolution of the AGN duty cycle with the prediction of the Menci et al. 2008 SAM. We see that this model reproduce the observed trend of increasing duty cycle from z$\sim$ 0 to z$\sim$ 5, although the observed AGN duty cycle at each redshift is somewhat smaller than predicted for the same stellar mass. We recall again that Compton thick AGN are present in the model, but a fraction may be missed in the data. This rough agreement suggests that the triggering of at least relatively luminous AGN (logL(2-10keV)$\gtrsim$43 ergs/s), is probably produced by galaxy interactions in the galaxy stellar mass and redshift range investigated (up to z$\sim 4-5$). At higher redshifts the model predicts a saturation of the AGN duty cycle of galaxies with masses log$M_* > 11.25$ $M_\odot$ (i.e basically all massive galaxies at z$\gtrsim$5 are expected to host an active nucleus with logL(2-10keV)$>$ 43 ergs/s).

5.1. Future perspectives

The faintest sources used in the comoving space density calculation are from the Chandra-GOODS-ERS sample. Indeed, we found that the HST/WFC3 ERS H band images are deep enough to trace high-z AGN populations at the extremely faint X-ray flux limits reached by the Chandra 4 Msec exposure, avoiding significant incompleteness, or at least with an incompleteness comparable to that reached at much brighter fluxes by Chandra-COSMOS and XMM-COSMOS. This is not the case for the HST/ACS optical and Spitzer IRAC images from which the GOODS-MUSIC catalog is generated. These images are too shallow to find the counterparts of all faint X-ray sources at the extremely deep CDFS 4 Msec flux limit. We conclude that to fully exploit ultradeep Chandra data, i.e. to keep the identification rate of faint X-ray sources comparable to that reached at brighter fluxes, a deep NIR (H$\gtrsim$26) coverage is mandatory. To avoid large incompleteness in the GOODS area without HST/WFC3 coverage we were forced to use only X-ray sources brighter than 5×10^{-17} erg/cm^2/s . It must be noted that the ERS area lies at relatively large off-axis angles in the Chandra field, where the sensitivity of Chandra is reduced by a factor of at least 2 by both vignetting and point spread function (PSF) degradation. As a result, we could not exploit in this work the full sensitivity of the 4 Msec Chandra field. This limitation can be overcome in future, when the HST/WFC3 CANDELS survey (Grogin et al. 2011; Koekemoer et al. 2011) will be ultimated. The CANDELS survey covers the central part of the Chandra field and therefore can allow us to fully exploit the Chandra sensitivity. Based on the ERS results we expect to at least double the sample of faint high-z AGN using the CANDELS survey of the CDFS.

The CANDELS multy-cycle HST treasury program covers a total of five fields: the CANDELS *deep* fields are in the GOODS-South and GOODS-North regions, and cover a total of 130 arcmin^2 to a depth of H=27.8. The CANDELS *wide* survey covers the AEGIS, COSMOS and UDS fields for a total of 670 arcmin^2 to a depth of H$\sim$ 26.5 (similar or slightly shallower than in the ERS field). All these five fields are going to be *premiere fields* for high-z galaxy and AGN studies. If we extrapolate our finding on the ERS field to all CANDELS fields, assuming a Chandra coverage of $\sim$ 4 Msec for the CANDELS *deep* fields and of $\sim$ 1 Msec for the CANDELS *wide* fields, we expect 30-100 z=4-5 AGN, 10-30 z=5-6 AGN and 3-10 z$>$ 6 AGN. This goal can be reasonably achieved by Chandra in the next few years (i.e. adding $\sim 5-6$ Msec of observation to $\sim$ 8 Msec already spent on these field). Probably the biggest problem with this sample would be the spectroscopic identification of these faint, high-z AGN. A fraction can be spectroscopically confirmed by HST/WFC3 grism spectroscopy. For the faintest, the only viable chances are probably ALMA observations in a few years, and, at the end of the decade, JWST and ELTs observations. At the end of this program we should have a very good knowledge of the faint end of the AGN luminosity function up to z=5, but a still rough determination of the luminosity function at z=5-7. To make further progresses with Chandra, i.e. quantitatively probe the first generation of accreting SMBH, which would allow putting stringent constraints on SMBH formation models (Madau & Rees 2001, Lodato & Natarajan 2006, Lodato & Natarajan 2007, Volonteri 2010, Volonteri & Begelman 2010, Begelman 2010), and accretion scenarios (Volonteri & Rees 2005, Dotti et al. 2010, Fanidakis et al. 2011, King et al. 2008), would require to at least triple the exposure times, i.e. spend on deep surveys other 30-40 Msec. While this is not technically unfeasible, it is certainly extremely expensive. The Chandra limiting problem is that its sensitivity is very good on axis, but degrades quickly at off-axis angles higher than a few arcmin, making difficult and expensive in terms of exposure time to cover with good sensitivity area larger than a few hundreds arcmin^2. A significant leap forward in the field would then be obtained by an instrument capable of reaching the Chandra Msec exposure, on axis sensitivity (i.e flux limits in the range $1-3 \times 10^{-17}$ erg/cm^2/s) but on a factor of >10 wider field of view. The extremely good Chandra PSF (HPD$\sim$ 0.5 arcsec), which is the main reason for the good Chandra sensitivity for point sources, is beyond reach of today technology of thin X-ray mirrors. However, this can be supplied for by increased throughput, lower background and wider field of view with nearly constant PSF. A straw-man calculation shows that a telescope with the total XMM throughput (i.e. area $\sim$half square meter) and a PSF $\sim$ 10 times worse than Chandra (i.e. HPD$\sim$ 5 arcsec) but slowly degrading with the off-axis angle, feeding a detector with half degree side and 2-3 time lower internal background would be as fast as Chandra but with a $\sim$ 20 times better *Grasp*, i.e. sensitivity times field of view. A further improvement could be achieved reaching an internal background similar to that of Swift XRT on low Earth orbit ($\gtrsim$10 times smaller than the Chandra internal background per unit solid angle).

The situation at the bright end of the luminosity function is fortunately easier. On this side, large areas will be surveyed in a few years by the XMM XXL survey and by eROSITA. The XMM XXL survey will cover $\sim$ 25 deg^2 of sky at a depth of $\sim 5 \times 10^{-15}$ erg/cm^2/s with 10 ks effective exposure. eROSITA will survey most of the sky down to a 0.5-2 keV flux limit $\sim 10^{-14}$ erg/cm^2/s , and hundreds deg^2 2-3 times deeper. The identification of high-

z AGN in these surveys requires near infrared follow-up. This will be possible with both present (VISTA) and future (Euclid) instrumentation. In particular, Euclid will provide H=24 photometry on most of the high galactic sky and H=26 photometry on about 50 deg^2. All these surveys will help in probing luminous AGN and test the completeness of the optical large area surveys such as SDSS. They will extremely useful to find rare high-z, high luminosity but highly obscured QSOs.

The present data can only put rough constraints on the high-z AGN duty cycle. We stress that the AGN duty cycle determinations are presented here for two main purposes: first we would like to point out that this measure as a function of the redshift is, at least in principle, a powerful tool to discriminate among different AGN triggering mechanisms. The present data show a fast increase of AGN duty cycle in massive galaxy with redshift, naively favoring galaxy encounters as triggering mechanisms. However, the uncertainties are still too large to draw any strong conclusion. Then, we use the AGN duty cycle determination to emphasize which are the main areas of improvement to reduce these uncertainties. First, we clearly need a better constrain on the AGN logL(2-10keV)=43-44.5 density at z$>$ 4. A major step toward this direction can be obtained by using further combined Chandra and HST surveys in the next few years. Second, we need better constraints on the galaxy stellar mass functions at z$>$ 3, in particular the low mass end of the mass functions. Efforts in this direction are on going, using both ground based surveys (with VISTA and other near infrared cameras on 8m class telescopes) and from the space (HST/WFC3 surveys and the Spitzer SEDS survey). Third, we need better constraints on the Eddington ratio distributions as a function of the redshift, in particular on the distribution at low L/L$_{Edd}$. Last, we need to test additional physics, such as BH gravitational recoil, and BH formation and growth in a *warm* DM scenario, through the comparison of model predictions with observed luminosity functions and AGN duty cycle. On going and future Chandra and HST surveys, in particular those planned in the CANDELS fields, should be able to find statistically sound samples of z=$\gtrsim$5 and logL(2-10keV)$>$ 43 AGN (a few tens), and put reliable constraints on the high-z galaxy stellar mass function, providing in turn much better constraints on the AGN duty cycle. Fig. 9 also shows the prediction of the Menci et al. 2006, Menci et al. 2008 SAM for low galaxy stellar masses (M$_*$ $\sim$ 10^{10} M$_\odot$). For such masses the duty cycle increase with the redshift, reach a maximum and then decreases at z$\gtrsim$4. This is due to the combination of two effects. First, small galaxies form in relatively low density regions, where gas cooling is slower, forming smaller gas reservoirs than for large galaxies. Second, at the highest redshifts the rate of galaxy interaction is small, it increases up to the redshift were groups forms and decrease again at low redshift because high relative velocities and low densities. The detection of this distinctive expectation would be the unambiguous confirmation of the galaxy interaction scenario for AGN triggering. While Chandra is sensitive enough to probe $\sim$ 10^7 M$_\odot$ SMBH up to z$\sim$ 7, the low mass end of the galaxy stellar mass functions at z$\gtrsim$4 is today practically unconstrained. The latter is therefore the area where improvements are more needed, but unfortunately also more difficult with the present generation of instruments. A breakthrough in this field would probably await for the next generation of infrared telescope such as JWST and the ELTs.

6. Summary

We have exploited the ultra deep Chandra and HST coverage of the CDFS to search for X-ray emission at the position of high redshift galaxies. To this purpose, we have used *ephot*, a highly optimized tool for X-ray source detection and photometry (see the Appendix). We found significant emission at the position of 17 galaxies in the area covered by the HST/WFC3 ERS survey, and 41 galaxies in the full GOODS area for a total of 54 independent z$>$ 3 X-ray sources, 29 of which are not present in previous X-ray catalogs. We reach a flux limit of $\sim 1.7\times10^{-17}$ erg/cm^2/s in the 0.5-2 keV band, which corresponds to luminosities of $\sim 10^{42}$ ergs/s at z=3 and $\sim 10^{43}$ ergs/s at z=7. The present Chandra deepest exposure is thus able to probe Seyfert-like galaxies up to the epoch of formation of the first galaxies and normal star-forming galaxies up to z=3-4. Indeed we have evidence that the X-ray emission of one of the faintest Chandra-GOODS-MUSIC source, M4417, is likely of stellar origin. This is the source in our sample with the lowest X-ray to H and z bands flux ratio, and the X-ray luminosity expected from the SFR rate measured from the UV rest emission, oxygen lines and radio 1.4 GHz emission is close to the observed one. This can be the highest redshift inactive galaxy observed in X-rays.

We analyzed the X-ray spectra of the Chandra-GOODS-ERS sources finding hard spectra in several cases. In 3 cases the spectra can be fitted with both a reflection model or an absorption model with a column density in excess 10^{24} cm^{-2}. In an additional case the column density results in the range $10^{23}-10^{24}$. The fraction of Compton thick AGN at 0.5-2 keV fluxes between 0.3 and 3×10^{-16} erg/cm^2/s and at z$>$3 is thus at least 18^{+17}_{-10}%. This is higher than predicted by popular models for the CXB (Gilli et al. 2007). Similar conclusions are reached by Gilli et al. 2011 and Treister et al. 2011. The optical counterparts of the highly obscured and Compton thick AGN do not show any reddening, and we thus conclude that the size of the X-ray absorber is likely smaller than the dust sublimation radius ($\lesssim$1pc, at the luminosity of our AGN).

We compared the X-ray spectra of the Chandra-GOODS-ERS and Chandra-GOODS-MUSIC sources with their optical spectra and optical/NIR morphology. Two Compton thick or highly obscured AGN show broad absorption lines in their UV rest frame spectra. Four of the ten highly obscured and Compton thick AGN have a point like morphology in their z and H bands images, thus suggesting that the active nucleus contributes significantly to the UV and optical rest-frame emission. Indeed, their rest-frame UV (0.16μm) extinction, estimated by fitting the observed SED with galaxy and AGN templates turns out smaller than 1-2 magnitudes in all cases. This implies that the X-ray absorber must be practically dust free, a condition satisfied if the X-ray absorbing matter is within or close to the dust sublimation radius. This is a fraction of pc for our sources, a region more compact than the pc-scale obscuring *torus*. Compact absorbers have been discovered in local Seyferts (e.g. Risaliti et al. 2005), they might be more common at high redshift.

We searched for radio emission at the position of the Chandra-GOODS-ERS and Chandra-GOODS-MUSIC sources in the deep VLA-CDFS maps at 1.4 GHz. We find highly significant emission (SNR>5) in 2 Chandra-GOODS-ERS sources and 5 Chandra-GOODS-MUSIC sources. We find radio emission with lower signal to noise (2.4<SNR< 3.2) in additional 8 sources in Table 3. The presence of significant radio emission from the faint X-ray sources is further confirmed by the analysis of the radio images obtained by stacking together the radio images at the position of Chandra-GOODS-ERS and Chandra-GOODS-MUSIC sources. The average flux per source of 6-10 μJy is higher than that expected by La Franca et al. 2011 based on the X-ray fluxes and assuming common nuclear origin. This would suggest either a strong evolution of the AGN radio "loudness" with the redshift (the La Franca et al. 2011 determination is mostly based on z< 3 AGN), or that our high-z, X-ray detected galaxies, are actively forming stars (SFR>a few hundreds $M_{\odot}$/yr). In two cases the SFR evaluated from the radio flux is consistent with that evaluated from sub-mm observations (M208) or UV SED fitting (M4417).

We evaluated the comoving space density of the z> 3 faint X-ray sources in three redshift bins: 3-4, 4-5 and > 5.8. We found that the wide luminosity range z> 3 luminosity functions are consistent with a pure luminosity evolution model, with L^* evolving quite rapidly, and reducing by a factor 3.3 from z=3 to z=6: $L^*(z = 3) = 6.6 \times 10^{44}$ ergs/s, $L^*(z = 6) = 2 \times 10^{44}$ ergs/s. We compared these space densities with the predictions of the Menci et al. 2006, Menci et al. 2008 SAM and with the expectations of more basic models for AGN activation through mergers. We find that these models are broadly able to reproduce the high-z AGN luminosity functions. A better agreement is found by assuming a minimum halo mass. We speculate that there are at least four effects or scenarios that can produce a minimum halo mass for BH formation and growth: 1) if BH are formed from the monolithic collaps of gas clouds, the probability for a DM halo of hosting a BH seed is an increasing function of the halo mass; 2) gravitational recoil, giving rise to ejection of one of the BH after a merging, which can be more important at low masses; 3) metallicity dependent star-formation; 4) a cut-off in the primordial power spectrum of gravitational perturbation at small scales. To assess the relative importance of all these effects we need *both* better data and more complete models for galaxy and AGN formation and evolution.

Finally, we empirically evaluated the evolution of the AGN duty cycle (fraction of AGN more luminous than 10^{43} ergs/s in the 2-10 keV band, to the total number of galaxies with the same mass) as a function of both host galaxy stellar mass and redshift. We compared it with the expectation of a model using galaxy interaction as AGN triggering mechanism. The uncertainties on the AGN duty cycle are large at all redshifts. At z< 4 they are dominated by the uncertainty on the Eddington ratio distributions. At higher redshift the uncertainty on both AGN luminosity function and stellar mass functions are extremely large, in particular at low AGN luminosities and small galaxy stellar masses. Nevertheless, it is clear how the AGN duty cycle must change substantially from z=0-0.5 to z=4-5, increasing by 1.5 orders of magnitude for host galaxy stellar masses $1 - 5 \times 10^{11}$ $M_{\odot}$. This big rate of change of the AGN duty cycle of massive galaxies is roughly consistent with that predicted by the models using galaxy interactions as AGN triggering mechanism. We recall again that this applies to relative luminous AGN (logL(2-10keV)$\gtrsim$43 ergs/s). Triggering of lower luminosity AGN is of course not constrained by our analysis.

Appendix A: *ePhot*: energy and space adaptive filter for source detection

The standard techniques for source detections identify statistically significant brightness enhancements, deriving from both unresolved (point) and resolved (extended) X-ray sources, in images accumulated in given energy ranges and observation times (such as tools 'celldetect', vptdetect' and 'wavdetect' in CIAO, 'emldetect' in SAS). However, binning and projection always result in a loss of information. Conversely, present X-ray data, and in particular Chandra/ACIS data, are incredibly rich, containing spatial, energy and timing information at very good resolutions. Even though X-ray data are organized in event files, preserving the information from the datacube, the scientific analysis is usually not performed directly on the original event files. The datacube is usually projected onto spatial plane before performing source detection, and spectra are accumulated at given times or at given sources positions before performing spectral fits. To take full advantages of large datacubes we should be able to detect sources in a multidimensional space. We are developing multidimensional source detection techniques using spatial, spectral and timing information. We search for clustering of X-ray events in a multidimensional space (energy and time in addition to the usual spatial coordinates). This allows us to efficiently detect X-ray bursty sources and X-ray sources characterized by a peaked spectrum (strong lines, cut-offed spectra), by reducing the elapsed time and/or the energy range (and therefore the background) where the source detection is performed.

We start by accumulating spectra at each galaxy position using different circular source extraction regions from 3 to 9 pixels on cleaned event files.

As first step we selected all galaxies with more that 12 background subtracted counts in the wide 0.3-4 keV band, to exclude the faintest objects, and achieve a high reliability (see Sect. A.2 below). At this stage the background is evaluated from a map obtained from the original image after the exclusion of all bright sources (sources detected by a wavelet algorithm at a conservative threshold).

For all these galaxies we search for the source extraction region radius and contiguous energy band that minimize the Poisson probability for background fluctuation and maximize the signal to noise ratio. We adopt a logarithmically spaced energy grid with width 0.025 dex from 0.3 to 6.5 keV.

Background at the position of each source is evaluated by normalizing an average background at the source off-axis to the source spectrum accumulated between 7 and 11 keV, where the contribution of faint sources is negligible, due to the sharp decrease of the mirror effective area. We do not use a 'local' background for two main reasons: 1) minimize the systematic error due to sharp background variations and 2) search for source detections in relatively narrow energy bands, where the 'local' background counts may be

Table A.1. Chandra background lines

Energy keV	Width keV	identification
0.585	0.05	Blend of Fe-L and O lines
1.49	0.015	1.4867 Al Kα(+1.5575 Al Kβ)
1.78	0.010	1.7400 Si Kα (+1.8359 Si Kβ)
2.16	0.045	Au M$\alpha\beta$
7.48	0.05	7.47 Ni Kα
8.26	0.16	8.28 Ni Kβ
9.71	0.06	9.71 Au Lα
11.5	0.1	11.44 Au Lβ
13.6-14	0.2	13.38 Au Lγ

small and the associated statistical uncertainty comparatively high.

A.1. Background evaluation

The study of faint X-ray sources requires the best possible characterization of the background. The typical level of the CDFS background in the 0.5-7 keV band is 2-3 counts/arcsec^2 or ∼25-40 counts in an area of 2 arcsec radius. The spectrum of the Chandra background is complex, with several broad and narrow components, both internal and of cosmic origin. To characterize the Chandra background we extracted its spectrum from the following regions: 1) circular region with radius 8 arcmin; 2) circular region with radius 3 arcmin; 3) annulus with internal radius 3 arcmin and external radius 6 arcmin; 4) annulus with internal radius 6 arcmin and external radius 8 arcmin. Circular region of 5 arcsec radius around all X-ray detected sources have been excluded from the analysis in all cases. Fig. A.1 shows the spectrum extracted from the broad 8 arcmin radius region. The continuum above a few keV is dominated by particle induced background (PIB), which has a power law shape with *positive* spectral index above 4-5 keV. Over-imposed to this continuum we see at least 8 strong emission lines. The best fit energies of the lines are and their identification is given in Table A.1. The rising background continuum and the strong emission lines present above ∼ 7 keV, coupled with the strongly decreasing mirror effective area above this energy, suggest to limit the analysis of faint sources to the band below 7 keV.

The low energy background spectrum is peaked at ∼ 0.5 keV and decreases rather sharply between ∼ 0.6 and ∼ 1 keV. This continuum and the 0.585 line suggest that this part of the background spectrum is dominated by the thermal emission from the local "superbubble". Below 0.3 the response of the instrument decreases sharply and therefore we limit the analysis at energies above 0.3 keV.

We have then fitted the background spectrum between 0.3 and 7 keV with a model including: 1) three gaussian lines to account for the features at 1.48, 1.74 and 2.16 keV; 2) one broad gaussian line to reproduce the broad bump between 1 and 3 keV; 3) two power laws modified at low energy by photoelectric absorption to reproduce the broad band hard continuum. All these components are not convoluted with the mirror effective area. 4) a thermal component with abundances fixed to Solar value, convoluted with the mirror effective area. This model provides a good fit to the background spectrum, without systematic residuals. We have then fitted the same model to the background spectra accumulated in three different regions, adjusting only the

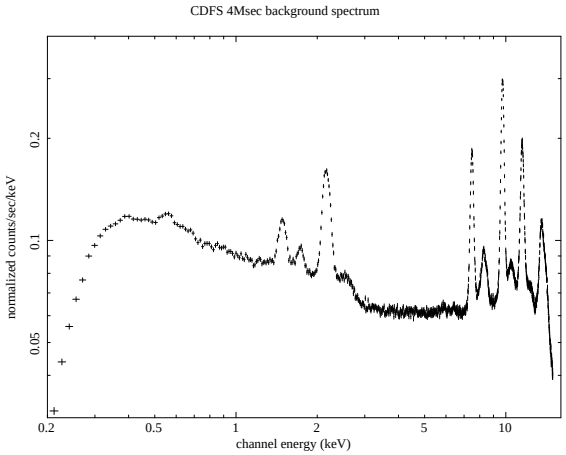

Fig. A.1. The spectrum of the background in the Chandra 4 Msec exposure of the CDFS. The spectrum has been extracted from a circle of 8 arcmin radius, after the exclusion of 5 arcsec radius region around all detected sources (10-20 arcsec for bright sources and extended sources).

global normalizations of the model spectra accounting for the internal and cosmic background components. The fits are remarkably good above 1 keV. Below this energy we see a deficit of counts in the 3 arcmin radius spectrum and in the 3-6 arcmin radius annulus spectrum, while there is an excess in the 6-8 arcmin annulus spectrum. The spectra become increasingly soft at large off-axis angles. The relative intensity of the thermal component is higher in the on-axis spectrum than in the off-axis spectrum, as expected if this component is truly cosmic, because of the larger mirror vignetting at high off-axis angles. The increase of the strength of the low energy cut-off at smaller off-axis is then probably due to a thicker deposition of contaminants at the centre of the ACIS-I 4 chip region.

The behavior observed for the emission lines is quite interesting. While the intensity of the 1.49 keV and 2.16 keV lines is constant with the off-axis angle, the intensity of the 1.78 keV Si line is larger at large off-axis angles.

The variations of the background spectra accumulated in thinner annuli becomes comparable with the statistical uncertainty. Guided by this analysis we decided to adopt the average background spectra accumulated in the three $r < 3'$, $3' < r < 6'$ and $6' < r < 8'$ in the following analysis.

To evaluate the background counts in each source extraction region we need to normalize the average background at three off-axis angles to that at each source position. To this purpose we first extract spectra from circular regions of 10 arcsec radii centered at each galaxy positions, and then normalize the average background to that in these spectra using the 7-11 keV faint-source-free band. The statistical uncertainty on the background evaluation is therefore mostly given by the 7-11 keV total number of counts at the source position. The choice of the size of the extraction region at each galaxy position must then satisfy two competing requirements. On one hand the region must be large enough to provide enough counts to keep statistical fluctuation small. On the other hand, a small region has the advantage of avoiding systematic errors due to sharp variations of the exposure time (and so of the background) typical of mosaics like the ACIS-I CDFS exposures, cosmetic defects, crowded regions with several sources within

few arcsec. The average CDFS 7-11 keV background in a 10 arcsec radius region is between 600 and 700 counts, $\sim$ 3 times higher than the 0.5-2 keV average background, 4 times the 1-2 keV background and 2 times the 1-4 keV background. Therefore, a circular region of 10 arcsec radius is a good compromise, because it collects a number of 7-11 keV counts similar or higher than the 0.5-2, 1-2 or 1-4 keV counts in 10-20 arcsec annulus (a typical region used to extract a 'local' background in crowded areas like the CDFS), in a three time smaller area.

A.2. Completeness, reliability and sky coverage

To extract statistically quantitative information from a given sample of "detected" sources we need to first assess its completeness and reliability (number of spurious detections). To this purpose we performed a series of extensive detection runs on simulated data.

First, to assess the reliability of our survey we performed simulations using background spectra only. We simulated about 10^5 spectra at the positions of the sources detected in the CDFS to use exactly the same exposure time, vignetting and PSF, but including only the average background at each off-axis position. We run our *ePhot* on these simulations and studied the number of spurious detections as a function of various parameters: 1) the threshold on background subtracted counts in a wide (0.3-4 keV) band; 2) the minimum and maximum source extraction regions; 3) the energy grid used to search for detections; 4) the bandwidth E_{max}/E_{min}; 5) the Poisson probability threshold for a source detection. We choose the combination of parameters that keep the number of spurious detections $\lesssim 1$ every 5000 spectra, i.e. the number of candidates in our search (see Sect. 2): 0.3-4 keV background subtracted counts ≥ 12, $E_{max}/E_{min} > 2$, Poisson probability $< 2 \times 10^4$.

To study the completeness of our survey we performed detection runs on simulated source plus background spectra. We used the Mock X-ray catalogs generated by R. Gilli, including about 10^5 AGN with a distribution of luminosities, redshifts and absorbing column densities in agreement with the Gilli et al. 2007 CXB model. In particular, the Mock catalogs include sources with unabsorbed flux down to 10^{-18} cgs, where the AGN density is $\sim$ 20000 deg^2. Source spectra are distributed over six templates, with column densities N_H up to 3×10^{24} cm^{-2}. A pure reflection spectrum is also considered to account for heavily Compton thick sources. The distributions of spectra is a strong function of both luminosity and redshift (see Gilli et al. 2007 for details). Using these Mock catalogs we simulated a 10 deg^2 Chandra survey with the same characteristics of the CDFS survey. We simulated sources at the position of the sources detected in the CDFS. We added to each simulated spectrum a background proportional to the average background at each off-axis angle. Finally, we run our on each source + background simulated spectrum our source detection algorithm *ePhot*. These simulations are used to study the completeness of our survey and compute the corresponding sky coverage. Fig. A.2, top panel, compares the 0.5-2 keV observed flux histogram of the simulated sources with that of the sources detected by *ePhot* with the thresholds defined above. The ratio of the two histograms gives the completeness of our survey, or the sky coverage, when normalized to the CDFS searched area. Fig. A.2, bottom panel, compares the *ePhot* sky coverage for the ERS area of the CDFS to that of a traditional detection algorithm at the same probability threshold (same fraction of spurious detection).

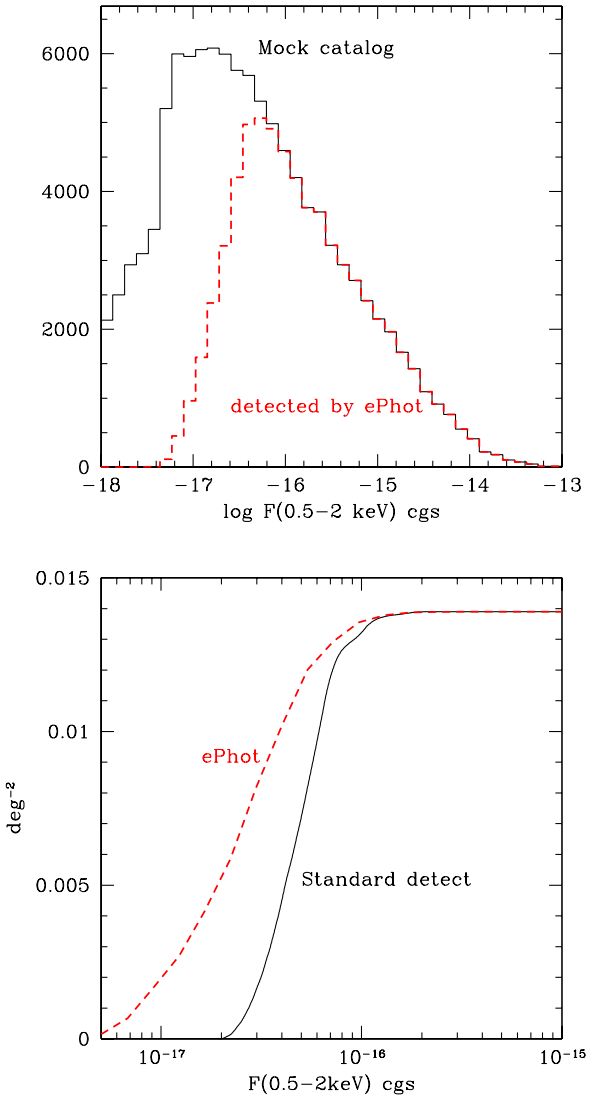

Fig. A.2. [Top panel:] the 0.5-2 keV flux histogram of the simulated sources (black solid histogram) and of the simulated sources detected by *e-phot*. [Bottom panel:] the Chandra sky coverage in the ERS area obtained using a standard detection algorithm (black solid curve) and using *e-phot* (red dashed curve) at the same probability threshold.

A.3. Photometry

e-phot was also run on the galaxy samples with fixed energy bands (0.5-2 keV, thus optimizing only for the size of the source extraction region). X-ray fluxes in the band 0.5-2 keV are estimated from *e-phot* count rates in the 0.5-2 keV band if the signal to noise ratio in this band is higher than 2.5 or from the count rates in the band that optimize the detection otherwise. A simple power law spectrum with $\alpha_E = 0.4$ has been assumed for the count rate flux conversion. To test our photometry we compared the 0.5-2 keV

flux obtained from the event files of the first 2 Msec observations to those in Luo08, and the 0.5-2 keV flux obtained form the full 4 Msec observations to those in Xue11. The agreement is remarkable, the median of the two samples agree within 3% and the semi-interquartile range of their ratio is 0.06. Fluxes of faint detections can be statistically over-estimated because of the so-called Eddington bias (Hogg & Turner 1998, Wang 2004). We estimated the bias according to Wang 2004 and found that it is at most $\sim$ 20% for our faintest detection and it is negligible for most of the Chandra-GOODS-ERS and Chandra-GOODS-MUSIC sources. Luminosities in Table 3 are calculated from fluxes corrected for the Eddington bias.

Acknowledgements

This work was supported by ASI/INAF contracts I/024/05/0 and I/009/10/0. FS acknowledges support from the Alexander von Humboldt Foundation. We thank R. Gilli for providing us with his mock catalogs of X-ray sources based on the GCH2007 model. FF thanks G.C. Perola, A. Comastri, M. Brusa, F. La Franca, G. Melini, R. Maiolino, E. Giallongo and H. Netzer for useful discussions. This work is based on observations made with NASA X-ray observatory Chandra. We thank the Chandra Director's office for allocating the time for these observations. X-ray data were obtained from the archive of the Chandra X-ray Observatory Center, which is operated by the Smithsonian Astrophysical Observatory. This work is also based data obtained with the NASA/ESA Hubble Space Telescope, obtained from the data archive at the Space Telescope Institute. STScI is operated by the association of Universities for Research in Astronomy, Inc. under the NASA contract NAS 5-26555. Observations were also carried out using the Very Large Telescope at the ESO Paranal Observatory under Programme IDs LP181.A-0717, ID 170.A-0788, and the ESO Science Archive under Programme IDs 67.A-0249, 71.A-0584, 69.A-0539.

References

Aird, J. et al. 2010, MNRAS, 401, 2531
Batcheldor D. 2010, ApJL, 711, 108
Barnes J.E., Hernquist L. 1996, ApJ, 471, 115
Begelman M.C. 2010, MNRAS, 402, 673
Best P.N., Kauffmann G., Heckman T.M., Brinchmann J., Charlot S., Ivezic Z., White S.D.M 2005, MNRAS, 362, 35
Boutsia K. et al. 2011, ApJ in press, arXiv:1104.5237
Bouwens R.J., Illingworth G.D., Blakeslee J.P, Franx M. 2016, ApJ, 653, 53
Bouwens, R.J. et al. 2010, arXiv:1006.4360
Brandt W.N. et al. 2004, arXiv:0411355
Brusa M. et al. 2009, ApJ, 693, 8
Brusa M. et al. 2009, A&A, 507, 1277
Brusa M. et al. ApJ, 2010, 716, 348
Bundy K. et al. 2008, ApJ, 681,, 931
Calzetti D. et al. 2000, ApJ, 533, 682
Caputi K.I., et al. 2011, MNRAS, 413, 162
Castellano M. et al. 2010, A&A, 524, 28
Cardamone C.N. et al. 2010, ApJS, 189, 270
Cavaliere A. & Vittorini V. 2000, ApJ, 543 599
Cen R. 2011, arXiv:1102.0262
Ciotti L., Ostriker J.P. 2007, ApJ, 665, 1038
Ciotti L., Ostriker J.P., Proga D. 2010, ApJ, 717, 708
Civano F. et al. 2011, ApJ in press, arXiv:1103.2670
Comastri A. et al. 2011, A&A, 526, L9
Cowie L. L., Barger A. J., & Hu E. M. 2010, ApJ, 711, 928
Daddi E. et al. 2007, ApJ, 670, 173
Dotti M., Volonteri M., Perego A., Colpi M., Ruszkowski M., Haardt F. 2010, MNRAS, 402, 682
Ebrero J. et al. 2009, A&A, 493, 55
Fanidakis, N., Baugh, C. M., Benson, A. J., Bower, R. G., Cole, S., Done, C., & Frenk, C. S. 2011, MNRAS, 410, 53
Feruglio C. et al. 2011, ApJL, 729, L4
Ferrarese L. & Ford H. 2005, Space Science Reviews, Volume 116, Issue 3-4, pp. 523-624, arXiv:0411247
Fiore F. et al. 2003, A&A, 409, 79
Fiore F. et al. 2008, ApJ 672, 94
Fiore F. et al. 2009 ApJ 693, 447
Fiore F. 2010, AIP Conference Proceedings, Volume 1248, pp. 373-380, arXiv:1002.3538
Fontana A. et al. 2006, A&A, 459, 745
Fontanot F., Cristiani S., Monaco P., Vanzella E., Nonino M., Brandt W.N., Grazian A., Mao J. 2007, A&A, 461, 39
Gallerani S. et al. 2010, A&A, 523, 85
Georgantopoulos I. et al. 2009 A&A 507, 747
Georgantopoulos I. et al. 2011, A&A, 526, 86
Genzel R. et al. 2006, Nature, 442, 786
Giacconi R. et al. 2002, ApJS 139, 369
Giallongo E., Fontana A., & Madau P. 1997, MNRAS, 289, 629
Gilli R., Comastri A., Hasinger G. 2007, A&A 463, 79
Gilli R., et al. 2011, ApJL, 730, L28
Glikman E., Djorgavski S. G., Stern D., Dey A. Jannuzi B.T. Lee K-S 2011, Apj, 728 L26
Grogin N. A. et al. 2011, ApJS, submitted, arXiv:1105.3753
Grazian A. 2010, submitted to A&A, arXiv:1011.6569
Grazian A. 2006, A&A 449, 951
Grazian A. 2010, submitted to A&A, arXiv:1011.6569
Haring N. & Rix H-W. 2004, ApJL, 604, L89
Hogg D. W. & Turner, E.L., 1998, PASP, 110, 727
Hopkins P.F., et al. 2006, ApJS 163, 1
Hopkins P.F., Richards G.T. & Hernquist L. 2007, ApJ 654, 731
Jiang L. et al., 2006, AJ, 132, 2127
Jiang L. et al., 2009, AJ, 138, 305
Kauffmann G. et al. 2003, MNRAS, 346, 1055
Kauffmann G. & Heckman T.M. 2009, MNRAS, 397, 135
Kelly B.C., Vestergaad M., Fan X., Hopkins P., Hernquist L., Siemiginowska A. 2010, ApJ, 719, 1315
King A.R., Pringle J.E., Hofmann J.A. 2008, MNRAS, 385, 1621
Koekemoer A. M. et al. 2011, ApJS, submitted, arXiv:1105.3754
Kollmeier J. A. et al. 2006, ApJ, 648, 128
Krumholz M.R., & Dekel A. 2011, submitted to ApJ, arXiv:1106:0301
La Franca F. et al. 2005, ApJ, 635, 864
La Franca F., Melini G., Fiore F. 2010, ApJ, 718, 368
Lamastra A., Menci N., Maiolino R., Fiore F., Merloni A. 2010, MNRAS, 405, 29
Lamastra A., Menci N., Fiore F., Di Porto C. Amendola L. 2011, MNRAS submitted
Lapi A., Cavaliere A., Menci N. 2005, ApJL, 619, 60L
Lapi A., Shankar F., Mao J., Granato G. L., Silva L., De Zotti G., Danese L., 2006, ApJ, 650, 42
Lodato G. & Natarajan P. 2006, MNRAS, 371, 1813
Lodato G. & Natarajan P. 2007, MNRAS, 377, L64
Luo B., et al. 2008, ApJS 179, 19 (Luo08)
Luo B., et al. 2010, ApJS 187, 560 (Luo10)
Madau P., Rees M.J. 2001, ApJL, 551, L27
Malkan M., Webb W., & Konopacky Q. 2003, ApJ, 598, 878
Marconi A. et al. 2004, MNRAS 351, 169
Maiolino R. et al. A&A, 2001, 365, 28
Maiolino R. et al. Nature, 2004, 431, 533
Maiolino R. et al. 2008, A&A, 488, 463
Malizia A., Stephen J.B., Bassani L., Bird A.J., Panessa F., Ubertini P. 2009, MNRAS, 399, 944
Mathur S. et al. 2001, New Astronomy, 6, 321
Mathur S., Wilkes, B.J., Gosh H. 2002, ApJL, 570, L5
Mathur S. et al. 2011, ApJ, submitted, arXiv: 1102.0537
McLure R.J. et al. 2011, MNRAS, 403, 960
McLure R.J. et al. 2011, MNRAS in press, arXiv:1102.4881
Menci N., et al. 2004, ApJ 604, 12
Menci N., et al. 2008, ApJ 647, 753
Menci N., Fiore F., Puccetti S., Cavaliere A. 2008, ApJ 686, 219
Merloni A., Rudnick G., Di Matteo T. 2004, MNRAS, 354, L37
Merloni A. & Heinz S. 2008, MNRAS, 388, 1011
Miller, N.A. et al. 2008, ApJS, 179, 114
Netzer, H. 2009, ApJ, 695, 793
Netzer, H. 2009, MNRAS, 399, 1907
Netzer H., & Trakhtenbrot B. 2007, ApJ, 654, 754
Norman C., et al. 2002, ApJ 571, 218
Panessa F. et al. 2006, A&A, 455, 173

Pannella M. et al. 2009, ApJL, 698, L116
Piconcelli, E., Bianchi, S., Guainazzi, M., Fiore, F., & Chiaberge, M. 2007, A&A, 466, 855
Primack J.R. 2009, AIP Conference Proceedings, Volume 1192, pp. 101-137, arXiv:0909:2021
Ranalli P., Comastri A., Setti G. 2003, A&A, 399, 39
Richards G. T. et al, 2006, ApJS, 166, 470
Risaliti G. et al. 1999, ApJ 522, 157
Risaliti G. et al. 2005, ApJ 623, L93
Schmidt, M. 1968, ApJ, 151, 393
Santini P. et al. 2009, A&A, 504, 751
Santini P. et al. 2011, A&A, submitted
Shen Y. 2009, ApJ, 697, 1656
Shankar F., & Mathur S. 2007, ApJ, 660, 1051
Shankar F. 2009, New A Rev., 53, 57
Shankar F., Weinberg D. H., & Miralda-Escudé J. 2009, ApJ, 690, 20
Shankar F., Bernardi, M. & Haiman, Z. 2009, ApJ, 694, 867
Shankar F., 2010, IAU Symposium, 267, 248
Shankar F., Crocce M., Miralda-Escudé J., Fosalba P., & Weinberg D. H. 2010a, ApJ, 718, 231
Shankar F., Weinberg D. H., & Shen Y. 2010b, MNRAS, 406, 1959
Shemmer O. et al. 2004, ApJ, 614, 547
Shemmer O. et al. 2004, ApJ, 644, 86
Shen Y. 2009, ApJ, 704, 89
Shi Y. et al. 2006, ApJ, 653, 127
Stark D.P. et al. 2009, ApJ, 697, 1493
Trakhtenbrot, B. et al. 2011, ApJ, 730, 7
Treister E. et al. 2010, ApJL, 722, L238
Treister E., Schawinski K., Volonteri M., Natarajan P., Gawiser E. 2011, Nature, 474, 356
Turner T. J., George I. M., Nandra K., & Mushotzky R. F. 1997, ApJS, 113, 23
van der Wel A. et al. 2011, ApJ, submitted, arXiv:1101.2423
Viel M. et al. 2008, Phys. Rev. Lett. 100.041304
Volonteri M. & Rees M.J. 2005, ApJ, 633, 624
Volonteri M., Lodato G., Natarajan P. 2008, MNRAS, 383, 1079
Volonteri M. 2010a, arXiv:1003:4404
Volonteri M. & Begelman M.C. 2010, MNRAS, 409, 1022
Volonteri M., Natarajan P., Gultekin K. 2011, ApJ in press, arXiv:1103.1644
Wang Q. D., 2004, ApJ, 612, 159
Willott C. J. et al., 2010a, AJ, 139, 906
Willott C. J. et al., 2010b, AJ, 140, 546
Windhorst R. A. et al. 2011, ApJS, 193, 27
Wyithe J. S. B., Loeb A. 2003, ApJ, 595, 614
Xue Y.Q. et al. 2011, ApJ in press, arXiv:1105:5643, Xue11
Yamada T. et al. 2009, ApJ, 699, 1354
Yun M.S., Reddy N.A., Condon J.J. 2001, ApJ, 554, 803